The Impact of GCM Dynamical Cores on Idealized Sudden Stratospheric Warmings and Their QBO Interactions

WEIYE YAO

Program in Atmospheric and Oceanic Sciences, Princeton University, Princeton, New Jersey

CHRISTIANE JABLONOWSKI

Department of Climate and Space Sciences and Engineering, University of Michigan, Ann Arbor, Michigan

(Manuscript received 17 August 2015, in final form 19 May 2016)

ABSTRACT

The paper demonstrates that sudden stratospheric warmings (SSWs) can be simulated in an ensemble of dry dynamical cores that miss the typical SSW forcing mechanisms like moist processes, land–sea contrasts, or topography. These idealized general circulation model (GCM) simulations are driven by a simple Held–Suarez–Williamson (HSW) temperature relaxation and low-level Rayleigh friction. In particular, the four dynamical cores of NCAR's Community Atmosphere Model, version 5 (CAM5), are used, which are the semi-Lagrangian (SLD) and Eulerian (EUL) spectral-transform models and the finite-volume (FV) and the spectral element (SE) models.

Three research themes are discussed. First, it is shown that SSW events in such idealized simulations have very realistic flow characteristics that are analyzed via the SLD model. A single vortex-split event is highlighted that is driven by wavenumber-1 and -2 wave–mean flow interactions. Second, the SLD simulations are compared to the EUL, FV, and SE dynamical cores, which sheds light on the impact of the numerical schemes on the circulation. Only SLD produces major SSWs, while others only exhibit minor stratospheric warmings. These differences are caused by SLD's more vigorous wave–mean flow interactions in addition to a warm pole bias, which leads to relatively weak polar jets in SLD. Third, it is shown that tropical quasi-biennial oscillation (QBO)–like oscillations and SSWs can coexist in such idealized HSW simulations. They are present in the SLD dynamical core that is used to analyze the QBO–SSW interactions via a transformed Eulerian-mean (TEM) analysis. The TEM results provide support for the Holton–Tan effect.

1. Introduction

In the winter stratosphere, the zonal-mean temperature field typically decreases from the tropics toward the pole, which is accompanied by a westerly jet in the midlatitudinal winter stratosphere. This causality is governed by the thermal wind relationship, and the zonal wind amplitudes of these ''polar night jets'' peak around 60°N/S in the upper stratosphere (around ≈1 hPa in nature). However, during some winters, the polar temperature occasionally increases rapidly over time, resulting in an increase in the zonal-mean temperature from 60° latitude toward the pole and the breakdown of the westerly jet. The 10-hPa temperatures at the pole can increase by 40–60 K in a week (Andrews et al. 1987; Schoeberl 1978). Such an event is called a sudden stratospheric warming (SSW), which was first discovered by Scherhag (1952). The event is considered a ''major warming'' if the 10-hPa zonal-mean zonal wind reverses to an easterly wind at 60° latitude. In cases where the 60° westerly jet at 10 hPa is strongly weakened but does not reverse, the SSW is called a ''minor warming.'' These SSW definitions follow the criteria suggested by the World Meteorological Organization (WMO CAS 1978, p. 36). However, as pointed out by Butler et al. (2015) many SSW detection criteria exist, which needs to be taken into account when comparing SSW statistics (McLandress and Shepherd 2009).

Corresponding author address: Weiye Yao, Program in Atmospheric and Oceanic Sciences, Princeton University, 300 Forrestal Road, Princeton, NJ 08544.
E-mail: weiye.yao@noaa.gov

DOI: 10.1175/JAS-D-15-0242.1

A sudden stratospheric warming is an important phenomenon that accounts for most of the climate variability in the polar stratosphere. In addition, extreme events like SSWs greatly impact the tropospheric circulation over subseasonal to seasonal time scales. This was first discussed by Baldwin and Dunkerton (1999, 2001) who noted that strong positive and negative anomalies of the annular mode at 10 hPa (an alternative measure of the strength of the polar vortex) often descend to the lowermost stratosphere and are followed by anomalous tropospheric weather regimes over the next one to two months. More specifically, the large stratospheric circulation anomalies can modulate the surface weather systems via changes of the midlatitudinal westerly wind amplitudes and the location of the storm tracks (Jung and Barkmeijer 2006). This implies that processes in the stratosphere influence the probability and positions of extreme weather events like high-wind midlatitudinal storms and the frequency of occurrence of high-latitude blocking and cold air outbreaks (Thompson and Wallace 2001). A better understanding and improved simulations of the stratospheric circulation and its interaction with the troposphere can therefore enhance the skill of extended-range tropospheric weather predictions (Jung and Leutbecher 2007; Sigmond et al. 2013). In the recent past, these influences of stratospheric events on the troposphere have been assessed quite intensely as, for example, documented by Gerber and Polvani (2009), Kodera et al. (2013), or Hitchcock and Simpson (2014). Other recent investigations also include the interaction between SSWs and the tropical quasi-biennial oscillation (QBO), the so-called Holton–Tan effect (Holton and Tan 1980), as discussed in Naito et al. (2003), Naito and Yoden (2006), Anstey et al. (2010), Garfinkel et al. (2012), Lu et al. (2014), Anstey and Shepherd (2014), or Watson and Gray (2014). In addition, various other forcings such as the sea surface temperature, the 11-yr solar cycle, El Niño, and La Niña events can influence the polar vortex and its QBO interactions (Baldwin et al. 2001; Wei et al. 2007; Richter et al. 2011).

SSWs are mainly generated and influenced by the upward propagation of tropospheric planetary (Rossby) waves and their interactions with the stratospheric mean flow (Matsuno 1971). Observations suggest that the onsets of SSWs could be related to atmospheric blocking events and the increased activity of easterly planetary waves (Naujokat et al. 2002; Martius et al. 2009; Woollings et al. 2010; Vial et al. 2013). Especially the zonal wavenumbers $s = 1, 2$ are most important for the SSW forcing (Matsuno 1971; Holton 1976). Zonal wind deceleration due to wave breaking near the critical level causes the transition from westerlies to easterlies during major SSWs and the descent of the critical level. The easterly zonal wind then blocks wave energy from further propagating upward and eventually reverses back to westerlies at a later stage of the SSW event (Holton 1976). In nature, planetary waves have larger amplitudes in the Northern Hemisphere than in the Southern Hemisphere owing to larger thermal and orographic forcing, causing stronger wave–mean flow interaction and thereby more frequent SSWs in the northern polar region (Andrews et al. 1987). Furthermore, the stratospheric temperatures at the South Pole are generally much lower than the temperatures at the North Pole (Manney et al. 2005). This might be a consequence of the larger (smaller) planetary wave forcing in the Northern (Southern) Hemisphere. The colder South Pole and enhanced meridional temperature gradients lead to a stronger stratospheric polar vortex, which is more difficult to reverse than the weaker polar jet in the Northern Hemisphere. As a consequence, only very few stratospheric vortex weakening events and only one major SSW in 2002 [as, e.g., analyzed by Manney et al. (2005) or Scaife et al. (2005)] have been observed so far in the Southern Hemisphere.

SSW simulations and predictions with atmospheric general circulation models (GCMs) have a long history. O'Neill (1980) and Grose and Haggard (1981) were among the first that successfully simulated spontaneously generated SSWs with coarse vertical ($\Delta z = 3\,\mathrm{km}$) and horizontal ($\Delta x > 300\,\mathrm{km}$) grid spacings. In addition, Simmons and Strüfing (1983) used the European Centre for Medium-Range Weather Forecasts (ECMWF) model to simulate an SSW event. Later examples of SSW studies with GCMs include the work by Erlebach et al. (1996), Manzini and Bengtsson (1996), Charlton et al. (2007), Marshall and Scaife (2010), and Coy and Pawson (2015).

Although SSWs have been successfully simulated in GCMs for decades, the factors that determine their initiation, evolution, and frequency are still not fully understood. Therefore, idealized SSW simulations are often utilized to unveil the dynamical processes of this phenomenon. Examples of these SSW investigations with dry dynamical cores can be found in Taguchi et al. (2001), Taguchi and Yoden (2002a,b), Kushner and Polvani (2005), Gerber and Polvani (2009), Sun et al. (2012), Domeisen et al. (2013), Jucker et al. (2013, 2014), and Sheshadri et al. (2015). All of these idealized GCMs use a Newtonian temperature relaxation and low-level Rayleigh friction to mimic the radiative forcing and boundary layer friction. Most often these idealized forcings were inspired by the ideas in Held and Suarez (1994), and modifications of the stratospheric equilibrium relaxation temperature have been introduced to create conditions with strong meridional temperature gradients in a single hemisphere (perpetual winter) or seasonally varying stratospheric relaxation temperatures. Note that the majority of the aforementioned investigators utilized idealized topography in their GCMs to force planetary waves, which contributed considerably to the forcing of SSWs. The only exceptions are Kushner and Polvani (2005) and Jucker et al. (2014) (their zero-topographic height $h = 0$-km experiment) who reported on very infrequent, spontaneously generated SSWs (approximately one every few thousand days) in their idealized GCMs without topographic forcing.

The idealized GCM simulations expose the dynamical interactions between the waves and the mean flow without the complexity of moisture processes, land–sea contrasts, or real topographic variations and make it easier to distinguish between causes and effects. However, none of the aforementioned investigators reported on simulations that are capable of simulating both idealized SSWs and QBO-like oscillations (Yao and Jablonowski 2013, 2015) in the stratosphere, which allows an assessment of their interactions. Therefore, we utilize a different idealized approach in this paper that lets us analyze the SSW processes and their interactions with the tropical stratosphere. As most other dry idealized studies, this alternative approach utilizes the Held and Suarez (1994) forcing in the troposphere but modifies the stratospheric temperature relaxation according to Williamson et al. (1998) [referred to as the Held–Suarez–Williamson (HSW) forcing]. The forcing is hemispherically symmetric, which leads to identical SSW statistics in both hemispheres. No topography, moisture, or seasonal cycles are used.

There are three main research themes in this paper, which are all centered around SSW events in idealized GCM simulations. First, we document the pure existence of minor and major SSWs in HSW model configurations and describe the properties of a single SSW event in the spectral-transform semi-Lagrangian (SLD) dynamical core of the Community Atmosphere Model, version 5 (CAM5) (Neale et al. 2010). The existence of SSWs with quite realistic properties could not necessarily be expected owing to the simplicity of the HSW model setup and the missing topographic forcing. So far, only the related zero-topography configurations by Kushner and Polvani (2005) and Jucker et al. (2014) had led to infrequent SSWs. These investigations provide insight into the SSW causes and effects that are driven by purely internal wave–mean flow interactions. Second, our study investigates the differences in the simulations in an ensemble of four GCM dynamical cores with identical HSW forcings. These are the four CAM5 dynamical cores: SLD, the Eulerian spectral-transform model (EUL), and the finite-volume (FV) and the spectral element (SE) dynamical cores. This sheds light on the impact of the numerical schemes and their diffusion characteristics on the physical phenomenon. Such an intercomparison is novel and has not been addressed in any of the other idealized SSW studies. Third, we explore the existence of tropical QBO-like oscillation in the presence of polar stratospheric jets and SSWs in the HSW configurations and use the SLD dynamical core to investigate their interactions.

The paper is structured as follows. The CAM5 dynamical core descriptions and the experimental setup are provided in section 2. Section 3 presents a brief overview of the SSW statistics over a 10 800-day simulation period and focuses on an in-depth investigation of a single SSW event in the SLD model. Section 4 intercompares the SSW statistics in the four CAM5 dynamical cores and sheds light on the SSW differences from a climatological viewpoint. Section 5 assesses the QBO–SSW link and discusses the QBO–SSW interactions in SLD. Conclusions are provided in section 6.

2. Description of the experimental setup

a. *The CAM5 dynamical cores*

We utilize the CAM5 modeling framework which has been jointly developed by the National Center of Atmospheric Research (NCAR) and various U.S. Department of Energy (DoE) laboratories. Four dynamical cores are used, which are the SLD, FV, EUL, and SE dynamical cores of CAM5. A detailed description of these can be found in Neale et al. (2010). The same dynamical cores have also been used in the two related QBO studies by Yao and Jablonowski (2013, 2015) that, for example, document the placement of the vertical levels. In particular, all models have 55 identical vertical levels with a model top at 0.1 hPa using a hybrid $\sigma-p$ (also called η) vertical coordinate with a variable vertical grid spacing. It spans from $\Delta z \sim 0.2$ km near the surface and increases with height in the troposphere. We select a constant $\Delta z = 1.25$-km vertical grid spacing in the stratosphere between 100 and 3 hPa and let the spacing increase to 2 km at the model top. The horizontal grid spacings for all dynamical cores are about $2° \times 2°$ or 220 km × 220 km in equatorial regions. This corresponds to the triangular truncation T63 in the spectral-transform models SLD and EUL. The numerical configurations are provided in Table 1, including the approximate horizontal grid spacing Δx at the equator, the dynamics time step Δt_{dyn}, physics time step Δt_{phys}, diffusion mechanisms, and the diffusion coefficient for

TABLE 1. Horizontal resolutions, approximate equatorial grid spacings Δx (km), dynamics Δt_{dyn} and physics Δt_{phys} time steps (s), and diffusion mechanisms with coefficients for each dynamical core. The T stands for triangular truncation and ne16np4 denotes that each cubed-sphere face is divided into 16 × 16 elements with $np = 4$ collocation points in each horizontal direction.

Dycore	Resolution	Δx	Δt_{dyn}	Δt_{phys}	Diffusion	Diffusion coefficient
SLD	T63	208	2700	2700	Implicit	—
EUL	T63	208	720	720	Fourth-order hyperdiffusion	$5 \times 10^{15}\,\mathrm{m^4\,s^{-1}}$
FV	2° × 2°	222	360	3600	Implicit and second-order divergence damping	Whitehead et al. (2011)
SE	ne16np4	208	540	2700	Fourth-order hyperdiffusion	$5 \times 10^{15}\,\mathrm{m^4\,s^{-1}}$

each model. All dynamical cores are built upon the hydrostatic and shallow-atmosphere approximation (the so-called primitive equations).

The SLD dynamical core (dycore) is a two-time-level, semi-implicit semi-Lagrangian spectral-transform model with a quadratic Gaussian transform grid with 192 × 96 grid points, which translate to a ~1.875° horizontal grid spacing (triangular truncation T63). The SLD dycore is used without explicitly applied horizontal diffusion. Its implicit numerical diffusion due to the semi-Lagrangian interpolations provides enough dissipation to avoid a buildup of kinetic energy near the grid scale. The damping effect of the cubic SLD interpolations mimics fourth-order horizontal hyperdiffusion (McCalpin 1988).

The FV dycore uses a gridpoint-based finite-volume discretization with an explicit time-stepping scheme and utilizes a regular 2° × 2° latitude–longitude grid. It is built upon a 2D shallow water approach in the horizontal (Lin and Rood 1996) and applies a vertical remapping approach to represent the vertical transport (Lin 2004). The vertical remapping algorithm conserves the total energy in the vertical column and is applied every ten dynamics time steps. FV's primary diffusion mechanisms are implicit numerical diffusion via limiters and explicitly applied second-order horizontal divergence damping (Whitehead et al. 2011; Jablonowski and Williamson 2011).

The EUL dycore is a three-time-level, semi-implicit Eulerian spectral-transform model in vorticity-divergence form with a T63 quadratic Gaussian transform grid (same as SLD). The EUL dycore is run with linear, explicitly applied fourth-order horizontal hyperdiffusion to maintain numerical stability. A leapfrog time-stepping algorithm is used with a Robert–Asselin time filter coefficient of $\alpha = 0.06$ (Asselin 1972).

The SE dycore is based on a continuous Galerkin spectral finite-element method and has been designed for fully unstructured quadrilateral meshes (Taylor and Fournier 2010; Dennis et al. 2012) on a cubed-sphere grid. SE employs an explicit Runge–Kutta time-stepping scheme. It is run at an "ne16np4" horizontal resolution, which is approximately equivalent to a 1.875° × 1.875° grid (see further explanations in Table 1). The SE dycore also uses a linear fourth-order horizontal hyperdiffusion mechanism with the identical diffusion coefficient than EUL.

We emphasize that the diffusion and filtering mechanism in the dynamical cores are tailored toward their numerical designs and have a large impact on the propagation and absorption of waves. This is especially true in the stratosphere that is typically characterized by phenomena with longer time scales in comparison to, for example, synoptic motions in the troposphere. A thorough description of the effects of diffusion, filters, and fixers on idealized atmospheric motions is provided in Jablonowski and Williamson (2011) and will be used to guide a future SSW sensitivity study.

b. *HSW forcing and sponge-layer friction*

The SSWs are simulated in HSW model configurations, which modify the Held–Suarez (HS) forcing (Held and Suarez 1994) in the stratosphere. The HS forcing consists of a Newtonian temperature relaxation toward a prescribed equilibrium state and Rayleigh damping of low-level winds. These processes mimic the effects of radiation and boundary layer friction. However, the HS forcing was designed to keep the stratosphere passive with an isothermal stratospheric relaxation temperature of 200 K. Therefore, a different stratospheric equilibrium temperature T_{eq} is introduced above the pressure level $p_d = 100\,\mathrm{hPa}$. As specified in Williamson et al. (1998) it is given by

$$T_{\mathrm{eq}} = T_0\left[\min\left(1, \frac{p}{p_d}\right)\right]^{R\gamma_d/g} + T_0\left\{\left[\min\left(1, \frac{p}{p_i}\right)\right]^{R\gamma_i/g} - 1\right\}, \tag{1}$$

where p symbolizes the pressure, $T_0 = 200\,\mathrm{K}$ is a reference temperature, $\gamma_d = 2\,\mathrm{K\,km^{-1}}$ denotes a lapse rate, $R = 287\,\mathrm{J\,K^{-1}\,kg^{-1}}$ is the ideal gas constant for dry air, $g = 9.80655\,\mathrm{m\,s^{-2}}$ stands for the gravity, and $\gamma_i = -3.345\,\mathrm{K\,km^{-1}}$ is a second lapse rate. The first term is effective when $p \le p_d$ and leads to a uniform decrease in temperature with height for all latitudes with lapse rate γ_d. The second term counteracts the first term in the tropics and becomes effective when $p \le p_i$. This causes a

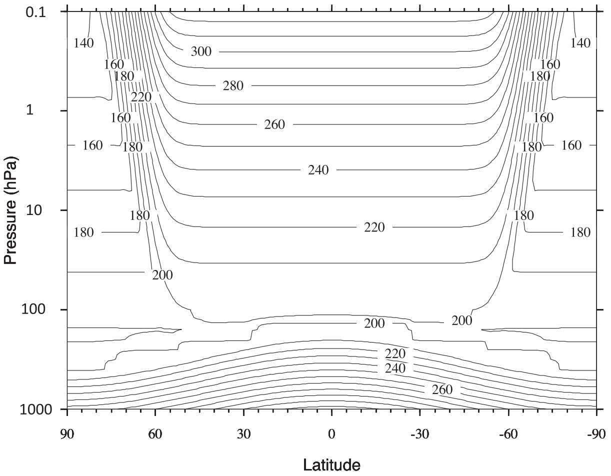

FIG. 1. Latitude–pressure cross section of the time-invariant HSW equilibrium temperature (K) with the parameter $p_{\mathrm{pl}} =$ 0.1 hPa.

temperature increase with height with the vertical temperature gradient $-\gamma_i$. The pressure threshold p_i depends on latitude ϕ and is defined as

$$p_i = p_{\mathrm{eq}} - (p_{\mathrm{eq}} - p_{\mathrm{pl}})\frac{1}{2}\{1 + \tanh[A(|\phi| - \phi_0)]\}, \quad (2)$$

where $p_{\mathrm{eq}} = p_d$, $p_{\mathrm{pl}} = 0.1$ hPa, $\phi_0 = \pi/3$ (corresponding to 60°), $A = 2.65/\Delta\phi_0$, and $\Delta\phi_0 = \pi/12$ (corresponding to 15°). In the original HSW setup, p_{pl} is set to 2 hPa. Here p_{pl} is modified to 0.1 hPa to adapt to the position of our higher model top. Such a change of the p_{pl} parameter was recommended by Williamson et al. (1998) for models with high model lids. The equilibrium temperature profile with $p_{\mathrm{pl}} = 0.1$ hPa is depicted in Fig. 1, which is identical to Fig. A1 in Williamson et al. (1998) below 3 hPa.

We apply additional Rayleigh friction to the zonal wind field near the model top between 1 and 0.1 hPa to absorb upward-propagating waves. This Rayleigh friction was also used in the related idealized QBO studies by Yao and Jablonowski (2013, 2015) to provide an upper-level sponge zone. This Rayleigh friction $\partial u/\partial t = -K_r u$ uses a pressure-dependent coefficient, which is given by $K_r = k_0\{1 + \tanh[(z - z_0)/H_0]\}$. The damping coefficient k_0 is set to $1/3$ day^{-1}, the log-pressure height is $z = h_0 \ln(p/p_0)$, the reference pressure p_0 is set to 1000 hPa, and h_0 stands for a scale height of 7 km. The quantity z_0 is set to 61 km, which denotes the approximate height position of the model top and the scale factor H_0 is 7.7 km. The friction leads to a damping time scale $1/K_r$ of about 41 days at 1 hPa and 2 days at 0.1 hPa. The HSW damping time scale of the Newtonian temperature relaxation is identical to the HS specification. It is 40 days except at low levels between $1 \geq \eta \geq 0.7$, where it varies between 4 and 40 days with latitude and pressure.

All HSW simulations are run for 10 800 days which we denoted as 30 model years where 1 model year corresponds to 360 days. This definition of a model year was also used in the related QBO studies by Yao and Jablonowski (2013, 2015). We therefore use both terms ''days'' and ''model years'' in the following discussion to more easily connect this paper to the idealized QBO investigations. The term ''month'' corresponds to 30 days.

3. Idealized SSW events in the SLD dynamical core

This section provides a short preview of the SSW statistics over the 10 800-day simulation period and mainly focuses on a selected SSW event in the SLD dynamical core. We thereby provide an in-depth assessment of an idealized SSW and its underlying dynamical principles. To put the SSW analysis into perspective, we first show the 10 800-day time series of the zonal-mean zonal wind at 60°–61°N and 9.3 hPa for all dynamical cores in Fig. 2. Note that a thorough model intercomparison is provided later. Here, we only briefly review the characteristics of the SLD model and use the reversal of the 60°N 10-hPa zonal-mean zonal wind to identify major SSWs in the Northern Hemisphere (Charlton and Polvani 2007). Figure 2 demonstrates that the zonal wind fields of all four dynamical cores exhibit strong westerlies with occasional collapses that indicate warming episodes. However, major warmings with zonal wind reversals are only found in the SLD dynamical core (in red) where they appear about 12 times in the 10 800-day record. Minor warmings in SLD are more frequent and occur about 25 times during these 30 model years.

a. *Description of a single SSW event in the SLD dynamical core*

We now shift the focus to a single major SSW event in the SLD dynamical core and document the wave activity during its life cycles. The selected event in model year 24 serves as an example. We picked it from the pool of the 12 major SSWs since it is a strong and long-lasting event. In addition, it is well isolated from any other minor or major SSW during the preceding 18–24-month time period.

Figure 3 shows several time series of this SSW event at the model level closest to 10 hPa (9.3 hPa) in year 24 (days 8760–8910). It depicts the 6-hourly instantaneous data from the SLD simulation. Figure 3a shows the zonal-mean zonal wind at 60.6°N and thereby represents

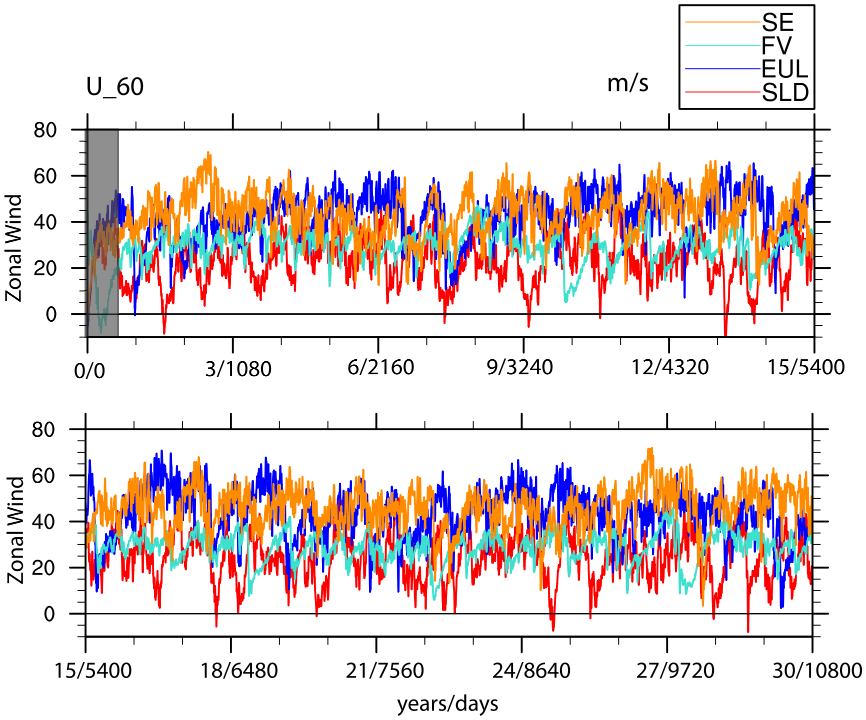

FIG. 2. The 10 800-day time series (based on 6-hourly instantaneous output data) of the zonal-mean zonal wind at 60°–61°N and 9.3 hPa for four dynamical cores: 60.6°N for SLD and EUL, 61°N for FV, and 60.5°N for SE. The spinup period is shaded in gray. Both the model years and simulation days are provided.

the strength of the mean polar vortex. The zonal-mean zonal wind is westerly with a speed around 30 m s^{-1} in the early phase before day 8785 before it starts to decrease and reverse to an easterly wind around day 8850. The fast portion of this zonal wind reversal happens between days 8840 and 8855 (first vertical line) when the wind speed drops by ~25 m s^{-1}. After a brief and weak westerly recovery period (days 8855–8868) the reversal of the now-easterly zonal-mean zonal wind stays in place for around 14 days (between days 8868 and 8882). Around day 8880 (second vertical line) the vortex recovery stage begins and the westerly polar vortex has fully recovered by day 8910.

Figure 3b displays the corresponding 9.3-hPa zonal-mean temperature near the North Pole (at 88.6°N), which is a good indicator of the polar stratospheric temperature. The zonal-mean temperature is rather steady around 205 K before day 8790 before a slow upward, partly oscillating, trend becomes apparent during the early development phase of the SSW. The fast polar temperature increase happens between days 8840 and 8850 when it increases from 205 to 240 K during this 10-day period. After this time during the mature SSW phase the polar temperature remains high for about 20 days (days 8850–8870) and drops back to 205 K by day 8910. The rapid polar temperature increases between days 8840 and 8850 exactly coincide with the rapid weakening of the westerly zonal flow (Fig. 3a) and consequent zonal wind reversal.

The evolution of the 9.3-hPa SLD meridional wind amplitude (at 60.6°N) of the zonal wavenumbers 1–3 is presented in Fig. 3c. This analysis provides information about the dominant wave drivers for the wave–mean flow interactions. As pointed out in Coy and Pawson (2015), the use of the meridional velocity emphasizes the higher wavenumbers more strongly than the typically used geopotential height. The zonal wave amplitudes of wavenumbers 1–3 are similar before the SSW event around day 8785. In the early SSW development phase (before day 8840), the peak amplitude of wavenumber 2 increases rapidly to around 20 m s^{-1}, and the wavenumber-1 amplitude oscillates between 3 and 8 m s^{-1}. During the SSW event from day 8840 onward, the peak wavenumber-1 amplitude drops to around 4 m s^{-1}, and the wavenumber-2 amplitude remains high around 20 m s^{-1} until day 8850. During the mature SSW stage (after day 8550), the wavenumber-2 amplitude decays rapidly and becomes comparable to the wavenumber-1 amplitude around day 8880, which marks the start of the vortex recovery

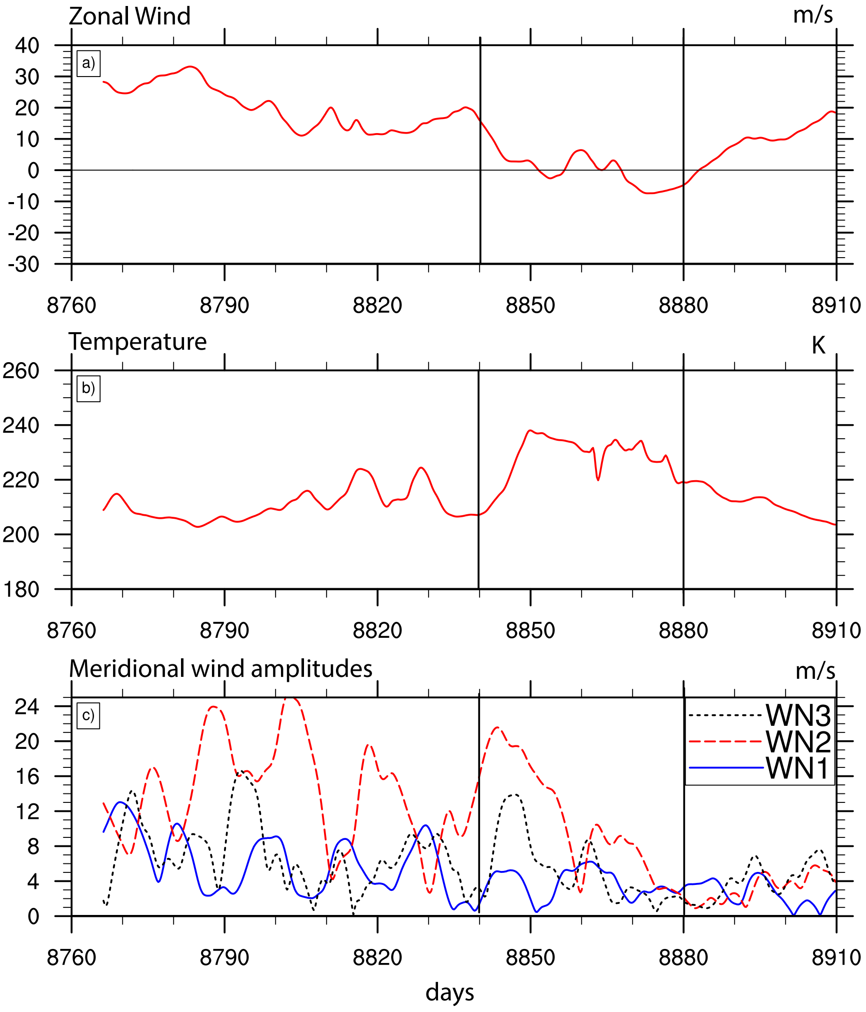

FIG. 3. Six-hourly instantaneous data at 9.3 hPa from the SLD simulation around model year 24 (days 8760–8910). (a) Zonal-mean zonal wind at 60.6°N ($m\ s^{-1}$). (b) Zonal-mean temperature at 88.6°N (K), and (c) 60.6°N meridional wind amplitudes ($m\ s^{-1}$) for zonal wavenumbers 1 (solid blue line), 2 (dashed red), and 3 (dotted black). The vertical lines at days 8840 and 8880 point to the start of the rapid development phase and the vortex recovery phase, respectively.

period. The wavenumber-3 amplitude oscillates before and during the SSW event and decays somewhat during the vortex recovery stage around day 8880.

Overall, the results imply that the wavenumber-2 forcing is the most important dynamical driver for this SSW event, followed by the wavenumber-1 forcing. This is typical for vortex-split events (Bancalá et al. 2012). Similar SSW characteristics have also been documented for complex GCM simulations by Coy and Pawson (2015, their Fig. 1). However, Coy and Pawson (2015) found a stronger zonal wavenumber-1 signal during the early development stages before the wavenumber-2 forcing dominated the vortex-split event in their simulations.

b. Analysis of the SSW category

In general, SSWs can be categorized as either vortex-split or vortex displacement events. As outlined in O'Neill (2003) and Charlton and Polvani (2007), a vortex displacement is characterized by a shift of the polar vortex off the pole and its following distortion into a comma-like shape. In a vortex-split event the polar vortex breaks up into two pieces of comparable size and magnitude. Figure 4 shows that the SSW event in the SLD dynamical core falls into the vortex-split category. In particular, the figure depicts a time series of the north-polar stereographic projection of Ertel's potential vorticity [EPV; see, e.g., Whitehead et al. (2015) for its hydrostatic definition]

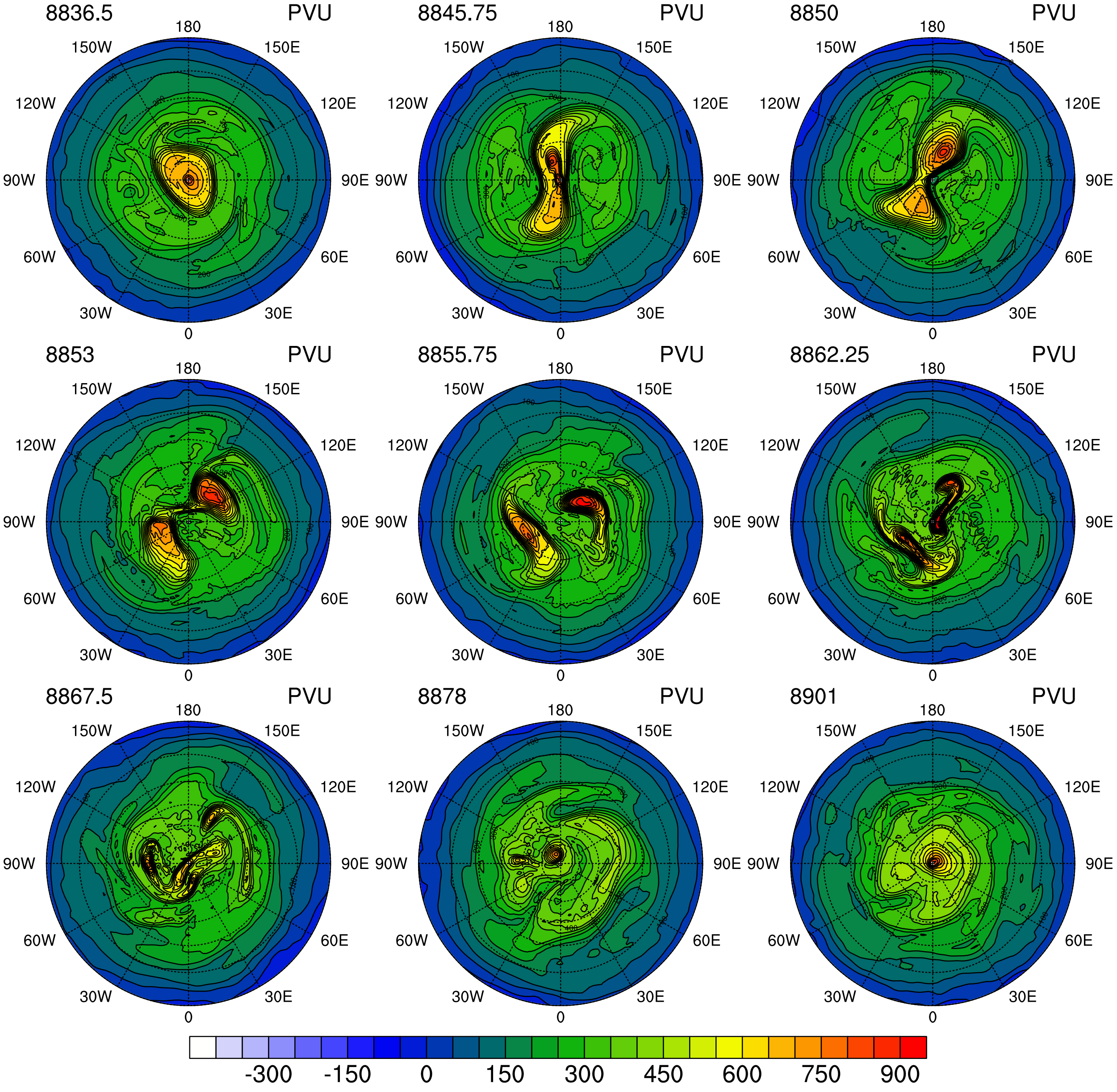

FIG. 4. Evolution of the Ertel potential vorticity on the 840 K isentrope (PVU) during the time period day 8836.5–8901 as labeled in the upper-left-hand corner of each panel. The north-polar stereographic projection of the SLD model is presented.

on the 840-K isentropic surface [in potential vorticity units (PVU); 1 PVU = $10^{-6}\,\mathrm{K\,kg^{-1}\,m^2\,s^{-1}}$]. The 840-K isentropic surface lies at about 10 hPa and thereby near the center of the polar vortex and is typically used for EPV analyses of SSWs (Manney et al. 2005; Coy and Pawson 2015). The EPV time sequence in Fig. 4 between days 8836.5 and 8901 captures all stages of the SSW event and is based on 6-hourly instantaneous SLD data. The EPV field has a circular shape around the North Pole at day 8836 before the SSW event and then starts to become distorted around day 8845 during the rapid development phase. The high-EPV center starts to split into two vortices during the mature stage from day 8850 onward and stays split for about 28 days before the recovery process follows from day 8878 onward. The single EPV maximum at the North Pole is finally reconstructed by day 8901. This EPV assessment is in good agreement with the 9.3-hPa analysis shown in Fig. 3.

c. *Wave analysis*

The initiation of SSWs is strongly affected by the planetary wave activity, which preconditions the

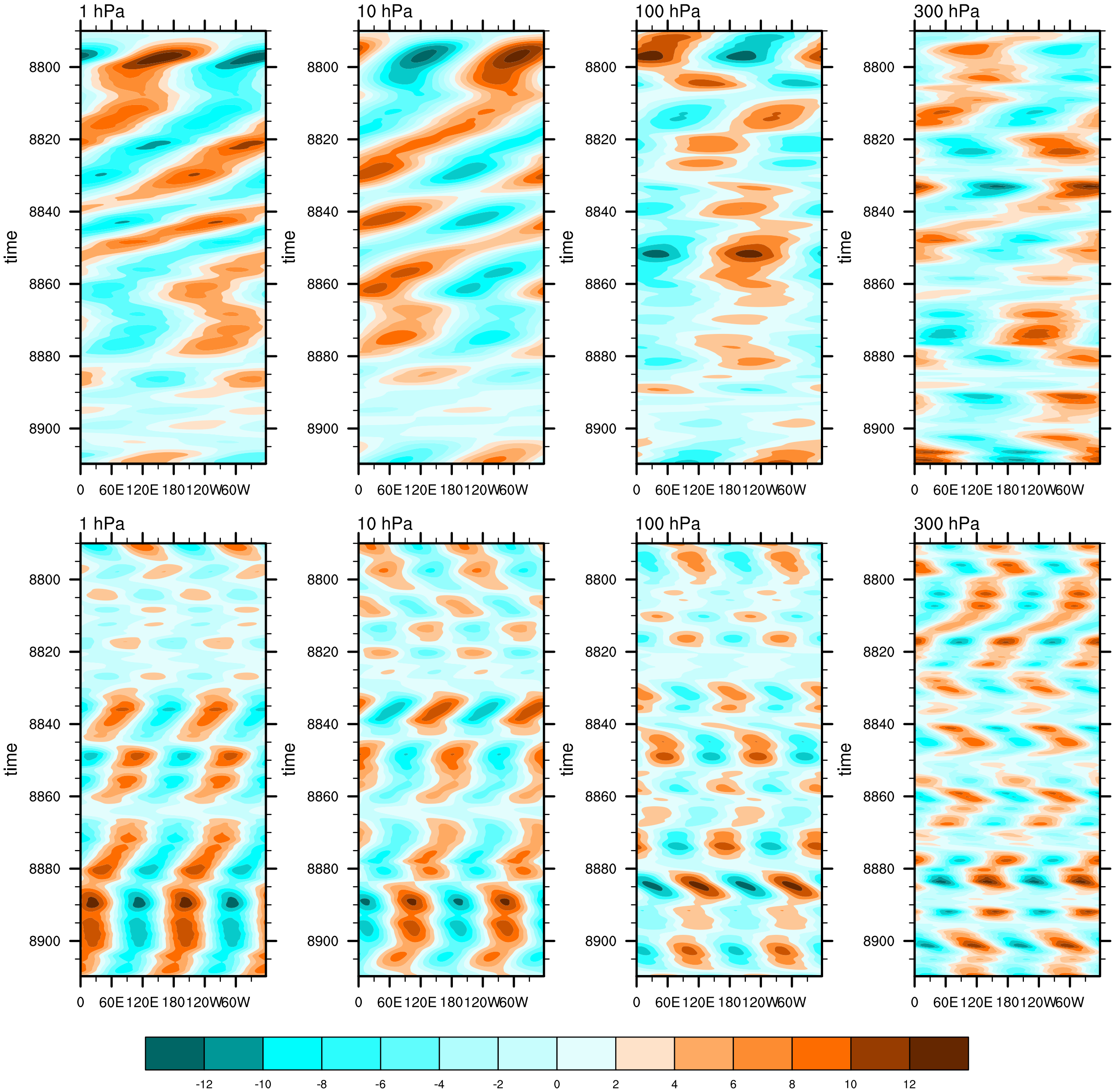

FIG. 5. Hovmöller diagram for wavenumbers (top) 1 and (bottom) 2 at (left to right) 1, 10, 100, and 300 hPa around model year 24. The result is obtained via Fourier analysis using 6-hourly SLD temperature anomalies at 60.6°N. The color scale shows the wave amplitude from −12 to +12 K in increments of 5 K. Time goes downward in each panel.

atmosphere. In particular, observational data have shown that planetary waves with zonal wavenumbers 1 and 2 play an important role for the SSW initiation (Naujokat et al. 2002; O'Neill 2003; Krüger et al. 2005). Moreover, anomalous upward Eliassen–Palm (E–P) fluxes from the troposphere into the stratosphere are observed right before and during the early stages of SSWs (Limpasuvan et al. 2004; Sun et al. 2012). The following Hovmöller analysis shows the wavenumber-1 and -2 activity to study the SSW initiation processes. In addition, transformed Eulerian-mean (TEM) analysis is used in the next subsection to shed light on the wave–mean flow interactions.

Figure 5 shows the Hovmöller diagrams of the wavenumber-1 (top row) and -2 (bottom row) components of the SLD temperature anomaly (deviations from the zonal mean) at 60.6°N using a fast Fourier transform method at the model levels closest to 1, 10, 100, and 300 hPa. The figures depict the same time period as shown before in Figs. 3 and 4 and are again based on

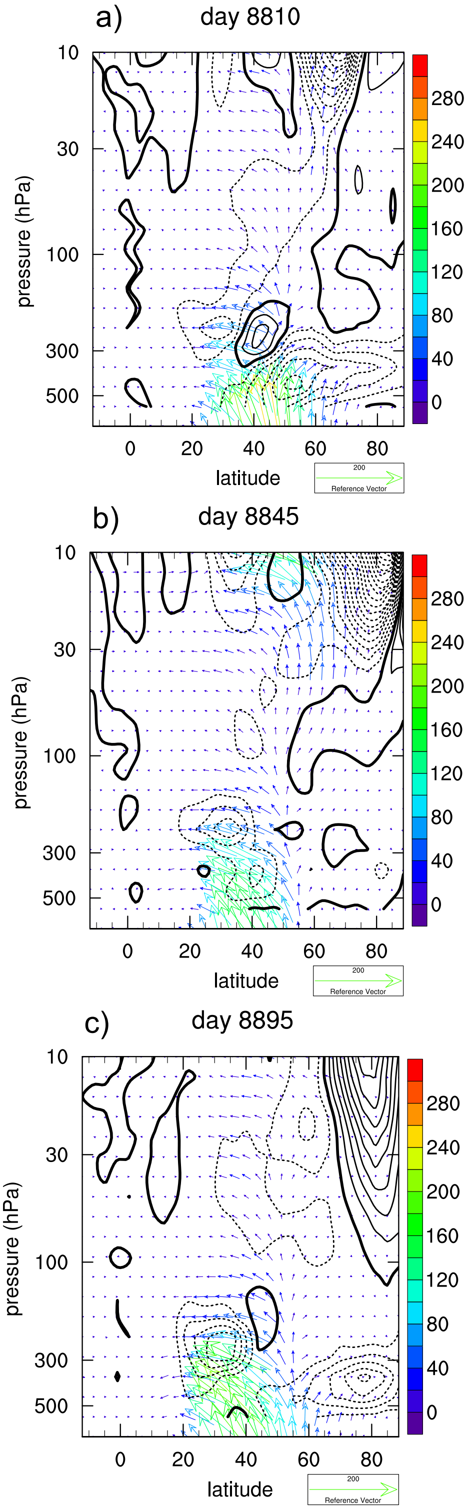

FIG. 6. Five-day-mean TEM analysis in the Northern Hemisphere using 6-hourly data from the SLD simulation. Vectors show scaled E–P flux vectors ($\mathrm{m^2\,s^{-2}}$), where the color denotes the magnitude. The background contours show the scaled divergence of the E–P flux (see text for scaling information) from -100 to $+40\,\mathrm{m\,s^{-1}\,day^{-1}}$ with an interval of $5\,\mathrm{m\,s^{-1}\,day^{-1}}$; negative contours are dashed, and the zero contour is denoted by the thick solid line. Five-day means are from (a) day 8810, (b) day 8845, and (c) day 8895 onward.

6-hourly instantaneous data. The time axis increases downward.

The wavenumber-1 components (top row) reveal that the 1- and 10-hPa levels are dominated by westward-propagating (easterly) waves throughout most of the simulation period with enhanced wave amplitudes before and during the SSW event (until day 8880). This westward forcing period at 1 and 10 hPa is only briefly interrupted by eastward-propagating (westerly) waves during a 10-day sequence between days 8860 and 8870. As it can be seen in Fig. 3a, this 10-day sequence approximately corresponds to the short and weak westerly recovery period of the zonal-mean zonal wind and the short downward spike of the polar temperature at day 8863 in Fig. 3b. Such a close correspondence suggests that the eastward-propagating (westerly) wavenumber-1 signals play a significant role in this 10–12-day irregularity of the SSW event before the polar vortex turns easterly again at day 8868. After day 8880 the westward amplitudes of the wavenumber-1 signals at 1 and 10 hPa diminish significantly, which marks the start of the vortex recovery period. Similar wavenumber-1 signatures are also present at 100 and 300 hPa but they are less organized and have lower phase speeds. However, the analysis at the lower levels suggests that a considerable portion of the waves originate in the troposphere and travel upward.

The wavenumber-2 components (bottom row) show weak eastward activity at the 1- and 10-hPa levels during the early simulation period until about day 8830, thereby counteracting the westward wavenumber-1 forcing. However, from day 8830 onward during the early development and mature stages of the SSW the wavenumber-2 propagation turns westward, thereby enforcing the mostly westward-propagating wavenumber-1 signals and causing the breakdown of the polar vortex. At the start of the vortex recovery period at day 8880 the wavenumber-2 signals at 1 and 10 hPa change character. They become stationary or tend to propagate slightly eastward which is even more pronounced at the 100- and 300-hPa levels after day 8880. Before day 8880 the wave forcing signals at these two lower levels are not as structured as the ones at 10 and 1 hPa. They exhibit frequent switches between eastward- and westward-propagating, or even stationary, wavenumber-2 signals.

In summary, before the SSW event wavenumber 1 is dominant in slowing/decelerating the westerly mean flow. As described in Labitzke (1981), this is a characteristic precondition for a major warming that is needed to change the zonal flow and to favor the propagation of wavenumber-2 signals. During the early and mature SSW stages wavenumber 2 becomes dominant in enforcing the easterly acceleration and reversing the polar vortex. Wavenumber 2 also dominates the vortex recovery process by providing most of the westerly acceleration after day 8880.

This raises the question what the wave generation mechanisms are in the absence of the typical wave triggering mechanisms like moisture processes, topography, or land–sea differences. This was also assessed by Scinocca and Haynes (1998), who used a very similar idealized GCM without any zonally asymmetric forcings or topography. They showed that the stratospheric variability in their model was solely driven by transient, baroclinic, and nonlinear wave–wave interactions that originated in the troposphere. These transient processes are a very likely wave source here. In addition, Yao and Jablonowski (2015) analyzed dynamic instability indicators in the upper troposphere as a potential triggering mechanism for equatorial waves. We therefore repeated such an analysis of the barotropic and baroclinic instability indicators in the polar–midlatitudinal region (not shown). Throughout the troposphere we find many occasions that fulfill the necessary conditions for barotropic and baroclinic instability, which can similarly act as a local wave trigger.

d. *Wave–mean flow interactions*

The Hovmöller diagrams can only reveal the existence of the dominant wave modes but do not quantify the resulting forcing. The impact of these wave modes on the mean flow can be analyzed via the divergence of the E–P flux vector ($\nabla \cdot \mathbf{F}$). In particular, we compute its body force $(a\cos\phi)^{-1}\nabla \cdot \mathbf{F}$ [see Edmon et al. (1980) for the quasigeostrophic definition in vertical pressure coordinates], which describes the acceleration of the zonal-mean zonal wind. The symbol $a = 6.37122 \times 10^6$ m stands for the radius of the earth. Figure 6 shows the scaled, quasigeostrophic E–P flux vectors and their divergence in the Northern Hemisphere during the life cycle of this SSW event in SLD. The figure depicts the early–preconditioning phase (day 8800), the mature phase (day 8855), and recovery stage (day 8885) of the SSW event. In particular, we scale the vectors using

$$(\tilde{F}_\phi, \tilde{F}_p) = \left(\frac{1000.0\,\text{hPa}}{p}\right)^{0.5} \times \cos\phi \left[\frac{(1/a)F_\phi}{s_\phi}, \frac{F_p}{s_p}\right], \quad (3)$$

where F_ϕ, F_p are the horizontal and vertical components of the E–P flux; $\tilde{F}_\phi$, $\tilde{F}_p$ are the scaled components of the E–P flux vector; p is the pressure in hPa; $s_\phi = \pi$ (radians) and $s_p = 10^5$ (Pa); and vectors above 100 hPa are further multiplied by a factor of 2 to emphasize the stratospheric pattern. This scaling technique is used for NCEP–NCAR E–P flux analyses by the National Oceanic and Atmospheric Administration (NOAA; see http://www.esrl.noaa.gov/psd/data/epflux/). The background contours in Fig. 6 denote the scaled divergence of the E–P flux (body force), with negative values dashed. The scaling factor $\sqrt{1000.0\,\text{hPa}/p}$ multiplies the E–P flux divergence to enhance the stratospheric features. At 10 hPa, this multiplicative factor is therefore 10. The E–P flux divergence and the vectors are averaged over a 5-day period to extract the main forcing signatures. The title of each plot lists the starting day of this 5-day averaging period.

During the preconditioning phase of the SSW event (Fig. 6a around day 8810) the divergence of the E–P flux is mostly negative in the stratosphere around 60°N. This means that the zonal wind acceleration due to wave–mean flow interactions is westward, which weakens the westerly polar vortex. At this time, the E–P flux vectors are mostly upward poleward of 50°N with moderate magnitudes that characterize upward-oriented eddy heat fluxes. During the mature stage (Fig. 6b around day 8845), the divergence of the E–P flux is strengthened in the stratosphere, which further accelerates the now developing easterly polar jet in SLD. The E–P flux vectors have higher magnitudes in the stratosphere as compared to the early stage, which indicates an increased upward eddy transport of heat and momentum. During the vortex recovering stage (Fig. 6c around day 8895), the divergence of the E–P flux in the stratosphere turns mostly positive (eastward) with rather weak upward eddy wave fluxes from the lower troposphere poleward of 50°N. This positive acceleration reestablishes the westerly polar vortex. The magnitudes of the scaled E–P flux divergence, which denotes the zonal wind acceleration, at 10 hPa show peak values around ±40–100 $\text{m}\,\text{s}^{-1}\,\text{day}^{-1}$, which correspond to unscaled values of ±4–10 $\text{s}^{-1}\,\text{day}^{-1}$. These forcing amplitudes are about a factor of 2–4 larger than the magnitudes in Limpasuvan et al. (2004, their Fig. 3), who documented a qualitatively similar SSW life cycle that was based on composites of daily mean NCEP–NCAR reanalysis datasets. Higher forcing magnitudes around ±10–15 $\text{m}\,(\text{s}\,\text{day})^{-1}$ have been reported by Martineau and Son (2013, their Fig. 3), who analyzed several SSW events with instantaneous ERA-Interim reanalysis data. Note that these comparisons are based on different time-averaging intervals and that reanalysis data are a model product with some uncertainties. These aspects contribute to a certain spread in the estimated forcing magnitudes. However, the forcing signatures are qualitatively similar.

4. SSW signals in four CAM5 dynamical cores

The previous section established that SSWs appear spontaneously in the idealized HSW simulations and that the SSW characteristics in the SLD dynamical core are quite realistic. The featured SSW event is driven by upward-propagating planetary waves that originate in the troposphere despite the absence of typical forcing mechanisms like moist processes, land–sea contrasts, or topography. We now evaluate the question whether the SSWs in the idealized simulations are impacted by the numerical schemes in various dynamical cores as we discovered in idealized QBO simulations (Yao and Jablonowski 2015). This sheds light on the internal wave generation mechanisms, the upward wave propagation characteristics, and their interactions with the mean flow, which are all influenced by the dissipation mechanisms in the dynamical cores. As described in section 2a we utilize the four CAM5 dynamical cores SLD, EUL, SE, and FV, which are examples of popular model design choices. We also encourage other modeling groups to contribute new HSW simulations to this intercomparison to further broaden the basis of the assessed numerical schemes. All analyses are based on instantaneous 6-hourly data for 10 800 days (30 model years).

a. SSW statistics

As before, we use the 60°N zonal-mean zonal wind to identify SSWs in the Northern Hemisphere as also suggested in Charlton and Polvani (2007). Recall that Fig. 2 displays the time series of the 9.3-hPa zonal-mean zonal wind closest to 60°N for each dynamical core (60.6°N for SLD and EUL, 61°N for FV, and 60.5°N for SE), which lets us now focus on the model intercomparison. All zonal wind fields exhibit strong westerlies with occasional collapses that indicate warming episodes. However, major warmings with zonal wind reversals are only found in the SLD dynamical core where they appear about 12 times in the 10 800-day record. No major warmings are apparent in the other three dynamical cores. The single major SSW in the model FV before month 9 occurs during the model spinup period and is, therefore, not counted. Although the zonal wind velocities of each dynamical core have strong fluctuations, the mean polar vortex in SLD is, on average, significantly weaker than the polar jets in FV, EUL, and SE. As an aside, the SLD vortex is also weaker than the observed Northern Hemisphere polar vortex, which makes its reversal easier. The 9.3-hPa zonal wind speeds in EUL and SE are the strongest with comparable maxima of over 60 m s^{-1}, followed by FV and SLD with typical maxima around 35 and 30 m s^{-1}, respectively. As shown below, these zonal wind maxima are closely connected to the typical meridional temperature gradients.

Despite the absence of major warmings in EUL, SE, and FV, they all show occasional periods with very weak polar jets (Fig. 2). This raises the question whether these time periods qualify as minor warmings. This is investigated in Figs. 7 and 8, which display the 10 800-day records of the 9.3-hPa zonal-mean temperature near the North Pole (88.6°N for SLD, EUL, and SE; 89°N for FV) and the 10-hPa zonal-mean temperature difference between 60°N and the North Pole. Most often, the polar temperature at 9.3 hPa stays close to a cold level, which is around 175 K for EUL and SE, 185 K for FV, and 205 K for SLD as seen in Fig. 7. This demonstrates that SLD has a much warmer polar temperature at 9.3 hPa than the other three dynamical cores, which is further investigated in section 4b. In case of an SSW event the polar temperature increases abruptly over the course of several (5–15) days. In the SLD simulation the polar temperature at 9.3 hPa rises to about 250 K in some of the SSW events, with a temperature increase of around 45 K. In FV the warm phases can reach 245 K with temperature increases by about 60 K. The SE simulation shows polar temperature increases of around 70 K with a temperature maximum of about 245 K during minor SSWs. The EUL simulation exhibits the strongest temperature increases of all simulations. As an example, the polar temperature rises to around 270 K during the minor SSW event between years 7 and 8. During other minor warming events in EUL the temperature often reaches 250–260 K, which indicates a sudden 75–85-K temperature increase. These are very large polar temperature fluctuations that even exceed the typical temperature rises of strong SSW events in nature. These are around 60 K as, for example, documented in Naujokat et al. (2002).

Figure 8 shows the related meridional temperature gradients at 9.3 hPa, using the zonal-mean temperature at 60°N minus the zonal-mean temperature at the latitude circle closest to the North Pole ($T_{60} - T_{\mathrm{pole}}$). These temperature differences are mostly positive and turn negative during the minor and major SSW events. Most often, the temperature difference changes more than 50 K over very short time periods as shown in Fig. 7. The new pieces of information provided in Fig. 8 are the vastly different magnitudes of the temperature gradients depending on the dynamical core. At 9.3 hPa the typical temperature differences in SLD are only about 20 K, which is in sharp contrast to the approximately 40 (FV) and 45 K (EUL, SE) in the other models. These significantly different magnitudes of the meridional temperature gradients partly explain the differing strengths of

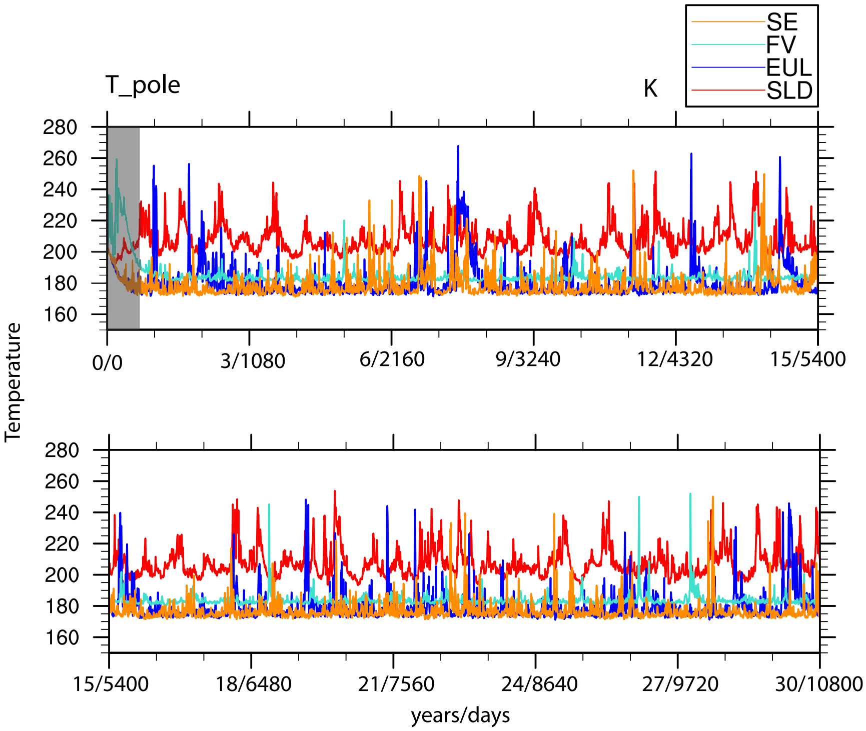

FIG. 7. The 10 800-day time series of the zonal-mean temperature (K) near North Pole (88°–89°N) at 9.3 hPa: 88.6°N for SLD and EUL, 89°N for FV, and 88.6°N for SE. The spinup period is shaded in gray. Both the model years and simulation days are provided.

the mean polar vortices seen in Fig. 2. Since the meridional temperature gradients are connected to the zonal winds via the thermal wind relationship a stronger gradient necessitates higher zonal wind speeds. However, this does not explain the rather small zonal wind difference at 60°N between SLD and FV in the presence of their vastly different temperature gradients. This apparent discrepancy is resolved in section 4b.

Figures 2 and 8 can also be used to estimate the counts of the minor and major SSW events in all four dynamical cores, which we define as the number of events with a $T_{60} - T_{\mathrm{pole}}$ temperature reversal (<0 K). In addition, major SSW events exhibit an easterly zonal-mean zonal wind according to the WMO detection criterion for SSWs. Using these criteria, SLD shows over 25 minor SSW events in addition to the 12 major SSW events identified earlier. FV is characterized by 5 minor warmings, EUL has about 17 minor warming events, and SE displays 12 minor SSWs in the 10 800-day time period when disregarding the 270-day spinup period. The very frequent occurrences of SSWs in SLD are related to its weaker meridional temperature gradients and slower zonal jet speeds. The results suggest that a strong anticorrelation between the zonal wind strength and the SSW frequency is present. This was also found by Jucker et al. (2014), who showed in their statistical analyses that stronger zonal-mean time-mean zonal winds make SSWs less likely. This suggests for our experiments that very little wave forcing is necessary to heat SLD's polar cap and to reverse its polar vortex in comparison to the other three dynamical cores. SE and EUL need to have the strongest wave forcings to collapse their strong polar vortices, which, on average, happens every 900 days or every 631 days, respectively. Interestingly, FV exhibits the fewest SSWs despite its lower barrier (lower polar jet speeds and higher polar temperature at 9.3 hPa) in comparison to EUL and SE. This is linked to a reduced wave activity in FV that provides a reduced forcing of the mean flow. Such a reduced wave activity in FV was also found in the tropical regions in the related QBO study by Yao and Jablonowski (2015) and is further analyzed in section 4c.

b. *Comparison of the general circulation*

The different SSW characteristics of the four dynamical cores and their typical zonal-mean zonal winds and temperatures (Figs. 2 and 7) at 9.3 hPa suggest that their climatic states in the stratosphere differ greatly despite the identical HSW forcing. To investigate this

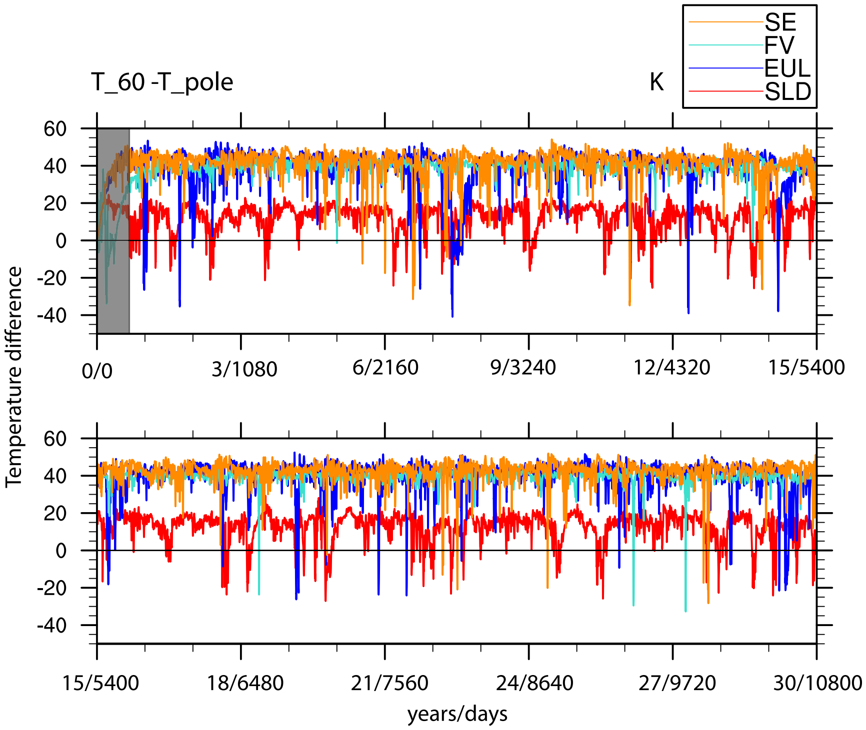

FIG. 8. The 10 800-day time series of the zonal-mean temperature gradient (K, $T_{60} - T_{\mathrm{pole}}$) between the midlatitudes (60°–61°N) and the North Pole (88°–89°N) at 9.3 hPa for SLD, EUL, FV, and SE. The spinup period is shaded in gray. Both the model years and simulation days are provided.

further, we present latitude–pressure cross sections of the 10 800-day-mean zonal-mean zonal winds (Fig. 9) and temperatures (Fig. 10) to highlight the general circulation of the four dynamical cores. This provides insight into the wide spread of the SSW statistics with the most numerous SSW events in SLD. As shown in Fig. 9, the tropospheric zonal jets are similar in all dynamical cores with maximum wind speeds around

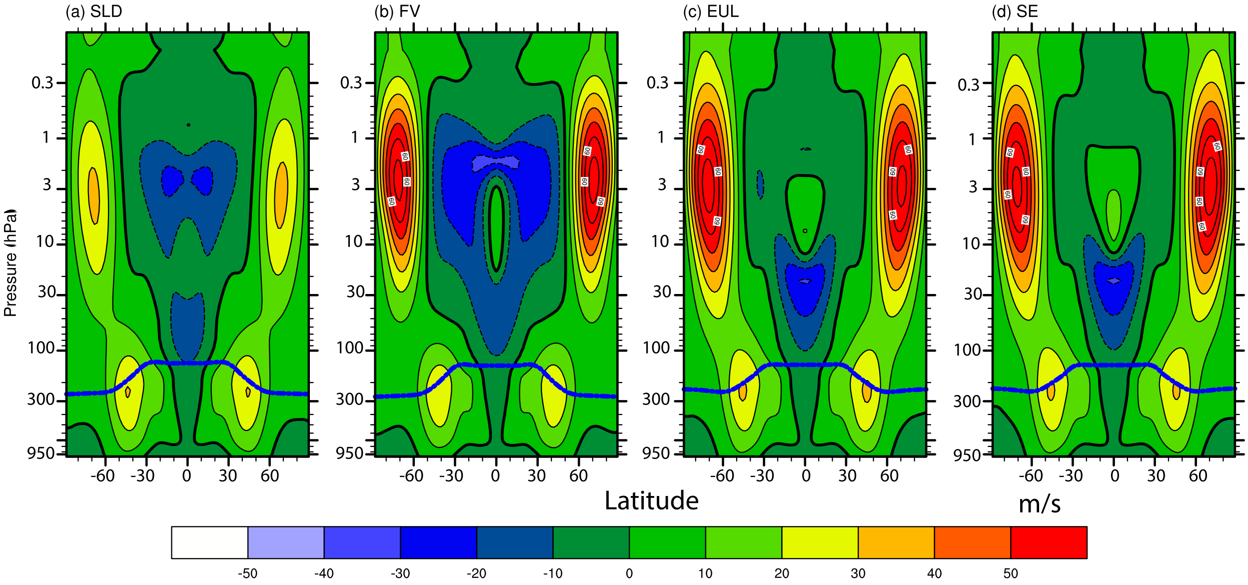

FIG. 9. Pressure–latitude cross section of the 10 800-day-mean zonal-mean zonal wind fields (m s^{-1}) in (a) SLD, (b) FV, (c) EUL, and (d) SE. The bold black line is the zero wind line. The heavy blue line indicates the tropopause position.

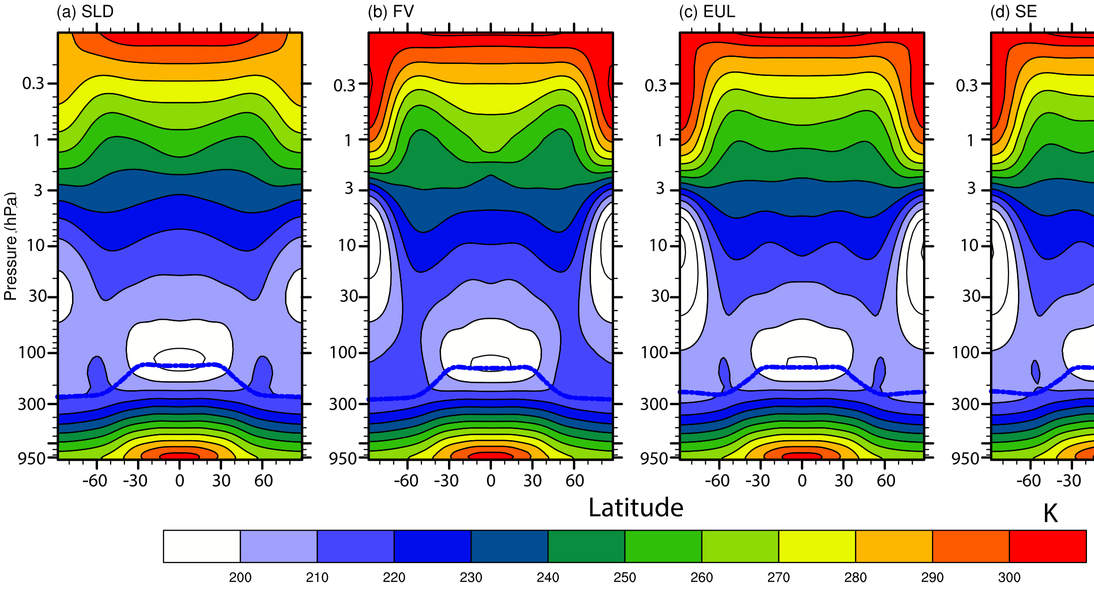

FIG. 10. Pressure–latitude cross section of the 10 800-day-mean zonal-mean temperature fields (K) in (a) SLD, (b) FV, (c) EUL, and (d) SE. The heavy blue line indicates the tropopause position.

30 m s^{-1} that are centered near 40°N/S at 250 hPa. In addition, the positions of the tropopause levels (using the lapse-rate-based WMO definition) in all models are also rather similar as displayed by the thick blue lines. However, the stratospheric zonal jets show significant differences. The SLD stratospheric polar jets have a maximum wind speed of around 30–35 m s^{-1}, whereas the peak polar jet speeds of other three dynamical cores are about 70 m s^{-1}. In addition, the SLD polar jets have lower-lying centers near 4–5 hPa, whereas the stratospheric jet centers of the other three dynamical cores are located at about 2–3 hPa.

The corresponding mean temperature fields of the four dynamical cores are presented in Fig. 10. As expected from the mean zonal wind (Fig. 9) and the 9.3-hPa temperature analyses (Figs. 7–8), the mean temperatures and their latitudinal gradients in the stratosphere are very different in SLD in comparison to the other three models. In particular, Fig. 10a shows that the cold spots in SLD's stratosphere lie near 30 hPa at the poles with minima around 195 K. In contrast, the centers of these polar cold spots lie close to 10 hPa with minima around 175–185 K in the other three dynamical cores. This downward vertical shift of the cold spots in SLD explains the vastly different base temperatures at 9.3 hPa near the North Pole in Fig. 7. In EUL, FV, and SE the polar temperatures in Fig. 7 reflect the temperatures of the cold pools, whereas the SLD values at 9.3 hPa record the increased temperatures above its low-lying cold spot. The vertical shift also explains the very different 9.3-hPa meridional temperature gradients (Fig. 8) and thereby the different polar jet speeds (Figs. 2 and 9), which are connected via the thermal wind balance.

The depictions of the general circulation also shed light on the apparent discrepancy between the 9.3-hPa wind speeds at 60°N and the magnitude of the meridional temperature gradients in SLD and FV. As discussed in section 4a the typical meridional temperature difference $T_{60} - T_{\mathrm{pole}}$ at 9.3 hPa (Fig. 8) in the absence of an SSW is about 20 K in SLD and 40 K in FV, but their mean westerly wind speeds at 60°N are rather similar with values around 20 (SLD) and 30 (FV) m s^{-1}. In contrast, EUL's and SE's mean $T_{60} - T_{\mathrm{pole}}$ temperature differences are around 45 K with mean zonal wind speeds of about 50 m s^{-1} at 60°N and 9.3 hPa. This raises the question why the FV model does not exhibit the high zonal wind speeds around 50 m s^{-1} as EUL and SE in the presence of an almost identical temperature gradient. The explanation lies in a slight, but systematic, poleward and upward shift of the polar jets in FV that pushes the strong westerly zonal jet speeds to slightly higher latitudinal and vertical positions. Therefore, the point measurement at 9.3 hPa and 60°N captures the equatorward flanks of the zonal jets in FV, which exhibits slower wind speeds around 30 m s^{-1} at this location. These issues with various SSW detection criteria have also been raised by Butler et al. (2015).

The systematic poleward shift of the westerly polar jets in FV is linked to the very different general circulation patterns in FV's stratosphere equatorward of 50° latitude. As Fig. 9b demonstrates, FV's stratosphere is largely dominated by strong easterlies, which was also observed in Yao and Jablonowski (2015) in their QBO studies when using the HS dynamical core configuration (their Fig. 3b). Here, Fig. 9 shows that the graphically enhanced zero wind lines between the easterlies in the midlatitudes and tropics and the westerlies in the polar regions extend to about 50°N/S in FV, whereas they lie closer to 45°N/S in EUL and SE with much-reduced easterly wind speeds. As a result, the high-latitude westerly jets in FV are pushed poleward.

The increased easterlies in FV's stratosphere are caused by the warmer temperatures in FV's midlatitudes. In particular, the SLD, EUL, and SE temperatures at 100 hPa and 60°N/S are about 200 K, whereas they are 210 K in FV in the same region that extends upward to 10 hPa. This results in larger latitudinal temperature gradients in the FV simulation and creates widespread easterlies in the lower stratosphere (Fig. 9b). In the upper stratosphere above 10 hPa, the stronger midlatitudinal north–south temperature variations further enforce the easterlies in FV. These stratospheric general circulation differences are striking when considering that all dynamical cores are forced in identical ways. It suggests that internal wave–mean flow interactions might be responsible for the differences, as further explored in the next subsection. In addition, numerical design differences, such as the dissipation properties of the dynamical cores, are likely contributors to these differences. The latter is briefly explored here before shifting the focus of the discussion to SSWs again.

Figure 10 shows that the SLD simulation exhibits a warm bias in the lower polar stratosphere between 3 and 100 hPa and a cold bias in the upper polar stratosphere from 3 hPa upward in comparison to the other three dynamical cores. Similar biases in the SLD model were also discussed by Williamson et al. (1998). They observed a warm SLD bias in the lower stratosphere in full-physics simulations with a lower model top (~2 hPa). The cold bias in the upper stratosphere was not seen, since their model configuration did not resolve the region above 3 hPa. Williamson et al. (1998) showed that an increase in the vertical resolution helps reduce the warm bias. Inspired by this idea, we doubled the vertical resolution in the SLD simulation (110 levels) and thereby halved the vertical grid spacing of our original 55-level setup. Figure 11 displays a randomly selected monthly mean zonal-mean SLD temperature snapshot that did not exhibit an SSW event. Note that the short averaging period (one month) leads to higher hemispheric asymmetries, which are irrelevant for the discussion here. As shown in Fig. 11, the reduced vertical grid spacing lessens the warm bias problem in SLD's lower stratosphere (Fig. 11). However, the cold polar center in SLD still lies lower at about 20 hPa, compared to 10 hPa in the other three dynamical cores. The cold bias problem in the upper stratosphere above 3 hPa is also decreased, but it is still lower than the temperature in the other three dycores by about 10 K at the model top. The reason why SLD has such a temperature bias in the stratosphere is not entirely clear but might be closely related to its very effective wave generation, propagation, and dissipation characteristics that also support QBO-like oscillations in the tropical stratosphere (Yao and Jablonowski 2013, 2015). Snapshots of these climatologically averaged wave–mean flow interactions are presented next.

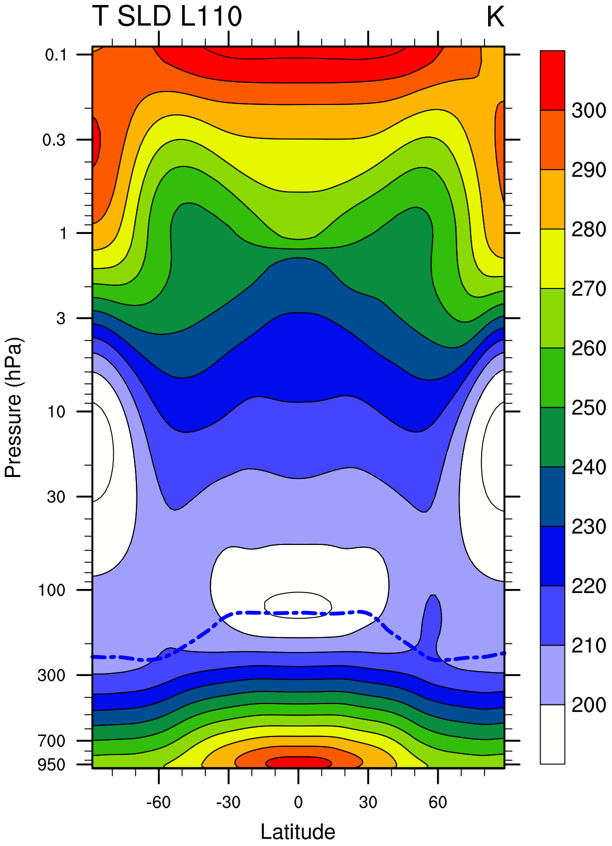

FIG. 11. Pressure–latitude cross section of the randomly selected monthly mean zonal-mean SLD temperature field (K) with 110 levels. The dashed blue line indicates the tropopause position.

c. Transformed Eulerian-mean analysis

To compare the averaged wave–mean flow interactions in all four dynamical cores, we perform a TEM analysis along constant pressure levels following Andrews et al. (1983). The analysis focuses on the mean climatic conditions instead of a particular SSW event in order to shed light on the different background flows in the HSW simulations. Figure 12 shows the unscaled

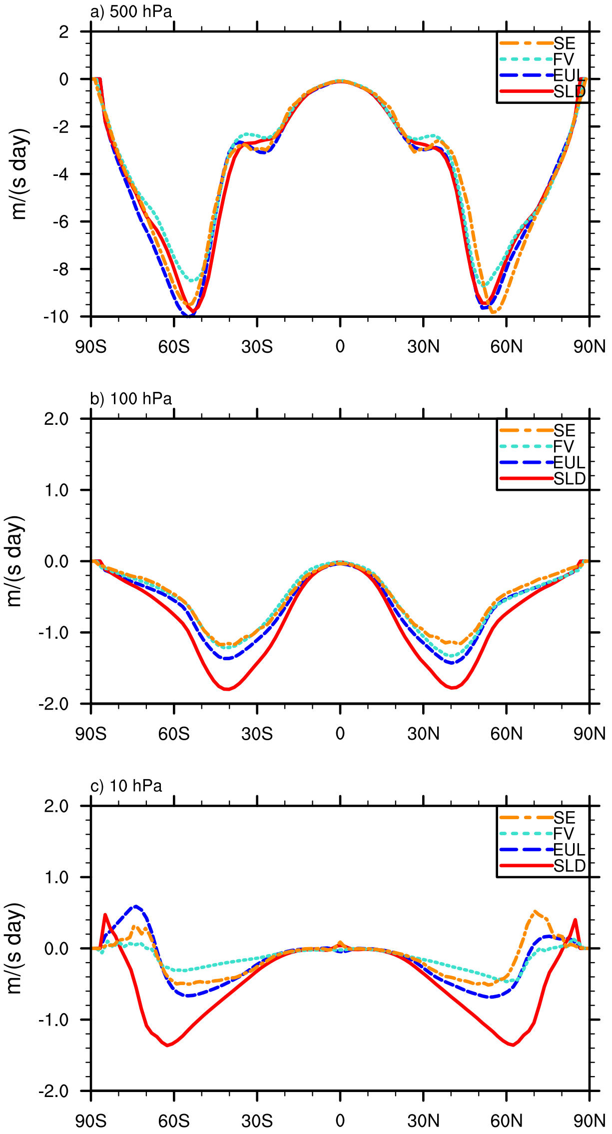

FIG. 12. Wave–mean flow interaction analysis using the TEM analysis. Thirty-month-mean zonal-mean divergence of the E–P flux (body force) at (a) 500, (b) 100, and (c) 10 hPa ($\mathrm{m\,s^{-1}\,day^{-1}}$) for SLD, EUL, FV, and SE.

30-month-mean zonal-mean divergence of the E–P flux (body force) at three different pressure levels in the four dynamical cores. The positive (negative) values indicate eastward (westward) zonal wind accelerations. At 500 hPa in Fig. 12a, the midlatitudinal wave accelerations are similar in all dynamical cores with maximum westward accelerations located near 55°N/S. The magnitudes of the westward accelerations are similar in SLD, EUL, and SE but slightly weaker in the FV simulation. These wave-driven forcings decelerate the westerly jets in the midlatitudinal troposphere. At 100 hPa in Fig. 12b, the westward (negative) zonal wind acceleration in SLD is significantly stronger in comparison to the other three models. The westward maxima of all dynamical cores lie at approximately 40°N/S, which are the latitudinal center positions of the jets in the upper troposphere/lower stratosphere. At 10 hPa the SLD dynamical core exhibits the strongest westward forcing, which is about twice as strong as the forcing in the model EUL and around 3 times as strong as the wave forcings in FV and SE. This forcing erodes the lower flanks of the westerly stratospheric polar jets in all dynamical cores. The increased amplitude of the westward forcing in SLD is therefore a decisive factor in the lower zonal wind speeds and decreased meridional temperature gradients in SLD's midlatitudinal–polar stratosphere. Overall, the wave forcing is weakest in the FV model at almost all levels. This suggests a reduced wave activity that is also reflected by the low SSW count in section 4a.

5. SSW and QBO interactions

The last discussion point in this paper addresses the interaction of stratospheric SSWs with other regions as mentioned in the introduction. Besides the fact that anomalies of the annular mode are often evident in the midlatitudinal troposphere and at the surface for some time after SSWs (Baldwin and Dunkerton 2001), SSWs also interact with the tropical circulation in the stratosphere. According to Holton and Tan (1980), SSW events are strongly impacted by the QBO phase. During an easterly QBO phase, the upward traveling planetary waves in the midlatitudes cannot enter the tropical regions and are confined or even redirected to the higher latitudes (Naito et al. 2003). Therefore, the Holton–Tan theory suggests that planetary waves are more easily directed toward the polar regions during easterly QBO phases, thereby favoring more SSWs. This can be investigated in HSW SLD simulations that simultaneously exhibit both SSWs and QBO-like oscillations.

a. Detection of QBO-like oscillations in HSW experiments

As shown in Yao and Jablonowski (2015) for HS simulations with an isothermal relaxation temperature in the stratosphere, all CAM5 dynamical cores, except FV, develop QBO-like oscillations in the tropical stratosphere, but with very different flow characteristics. Therefore, we first investigate whether QBO-like oscillations are still present in HSW experiments and whether they differ from the HS simulations in Yao and Jablonowski (2015).

Figure 13 displays the 10 800-day (30 model years) HSW time series of the monthly mean zonal-mean zonal

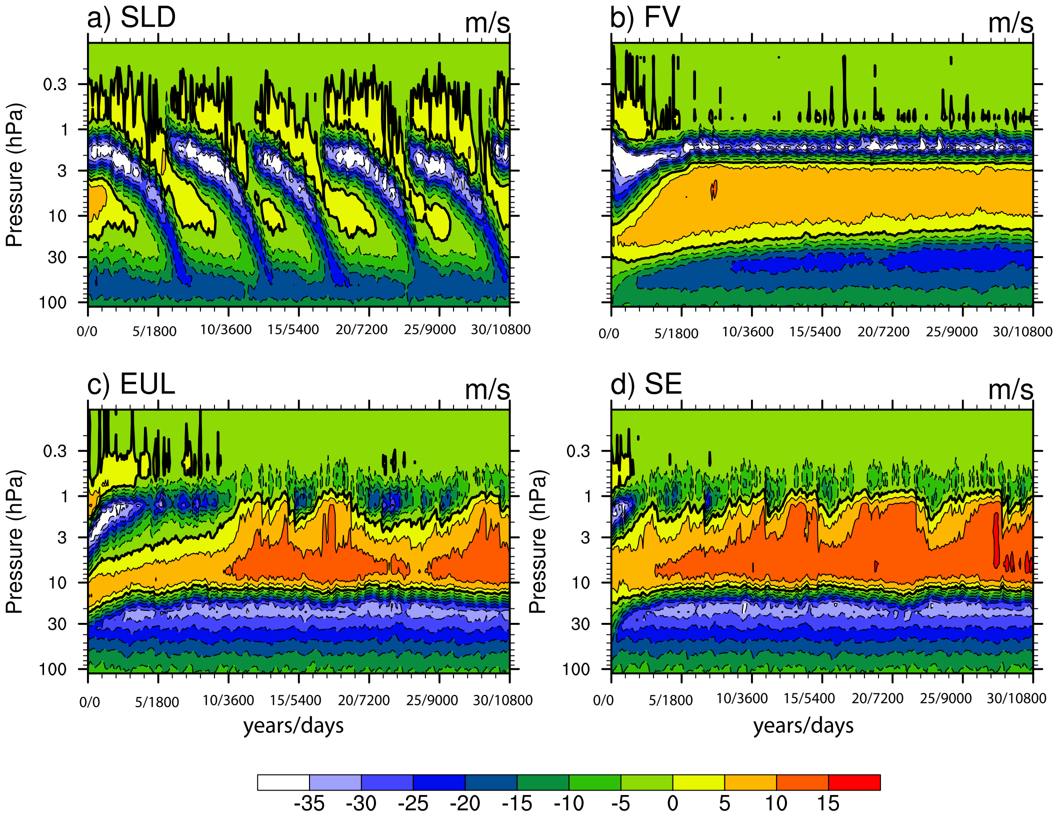

FIG. 13. The 10 800-day time series of the monthly mean zonal-mean zonal wind ($\mathrm{m\,s^{-1}}$) at the equator for different dynamical cores, averaged between ±2°: (a) SLD, (b) FV, (c) EUL, and (d) SE.

wind at the equator (averaged between ±2°) for all four dynamical cores. The figure shows that a QBO-like oscillation with switching westerlies and easterlies is present in the SLD dynamical core (Fig. 13a), which occupies the upper stratosphere between 1 and 50 hPa. When compared to the HS simulation with SLD in Yao and Jablonowski (2013, 2015), the QBO-like oscillation in the HSW SLD simulation has a longer period (6 model years in HSW versus 3.6 model years in HS), reduced westerly and increased easterly wind magnitudes (from −40 to under 5 $\mathrm{m\,s^{-1}}$ in HSW versus from −35 to over 10 $\mathrm{m\,s^{-1}}$ in HS), and overall very weak westerly QBO phases that only propagate down to about 20 hPa (30 hPa in HS). As found before in Yao and Jablonowski (2013, 2015), the average QBO periods in SLD are too long in the idealized simulations in comparison to observations [28 months; see Baldwin et al. (2001)].

Figures 13b–d depict the corresponding zonal winds at the equator of the other three dynamical cores. As also documented in the HS simulations in Yao and Jablonowski (2015), the FV dynamical core with the HSW forcing (Fig. 13b) is not able to establish a QBO-like oscillation. An easterly jet with a peak wind speed of −35 $\mathrm{m\,s^{-1}}$ occupies the levels between 1 and 3 hPa, a westerly jet around 5 $\mathrm{m\,s^{-1}}$ is located between 3 and 30 hPa, and another easterly jet is established in the lower stratosphere below 30 hPa. An unexpected result is that the HSW simulations with EUL and SE (Figs. 13c,d) lose their QBO-like oscillations that were present in HS model configurations (Yao and Jablonowski 2015). The simulation results for EUL and SE are very similar. A westerly wind regime with an amplitude of about 10 $\mathrm{m\,s^{-1}}$ occupies the region between 1 and 10 hPa, and an easterly jet with about −30 $\mathrm{m\,s^{-1}}$ is located below 10 hPa. However, the westerly wind regimes in EUL and SE are far from regular, which suggests that easterly wave forcings try to break through the westerlies but with insufficient strengths. The easterly forcing thereby put dents into the westerly flow but fails to reverse it.

b. The Brewer–Dobson circulation

It is interesting that the new HSW relaxation temperature with its strong meridional gradients near 60°N/S modifies the tropical QBO-like oscillations quite significantly. One explanation points to the increased strength of the Brewer–Dobson circulation in the presence of polar jets, which do not develop in HS simulations (Yao and Jablonowski 2015). Figure 14 briefly

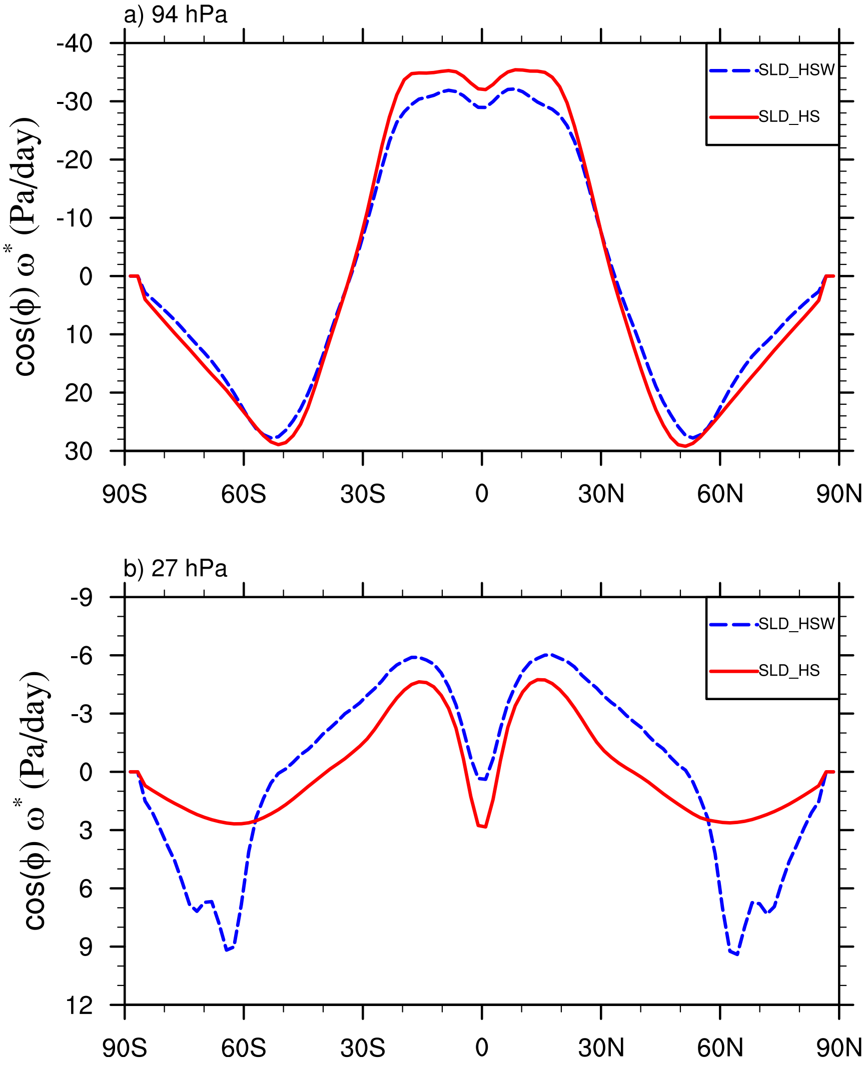

FIG. 14. Latitudinal profiles of 30-month-mean, zonal-mean, area-weighted vertical pressure velocities $\overline{\varpi}^* \times \cos\phi$ of the residual circulation for SLD simulation with HS and HSW forcing at (a) 94 and (b) 27 hPa.

investigates this aspect. It shows the area-weighted 30-month-mean zonal-mean residual vertical pressure velocity ($\overline{\varpi}^* \times \cos\phi$) that represents the strengths of the Brewer–Dobson circulation. Here, the SLD analyses at the 94-hPa tropopause level and within the QBO regime at 27 hPa are shown for both the HS and HSW forcing. The HS results are replicated from Yao and Jablonowski (2015, their Fig. 6). The 30-month averaging periods cover the years 7.1–9.6 (HS) and 2–4.5 (HSW).

Figure 14a shows that the upwelling (negative pressure velocities) at the tropopause level in HS is slightly stronger than that in the HSW simulation in the tropics. Other regions are almost indistinguishable. However, within the QBO domain at 27 hPa the residual circulations in HS and HSW are quite different. The HS simulation is dominated by downwelling near the equator and poleward of ±40° and upwelling in the regions between 5° and 40°N/S. In contrast, the HSW circulation is characterized by upwelling throughout the tropics (except at the equator between ±1°) and the midlatitudes until about 55°N/S and downwelling poleward of approximately 55°N/S. This HSW Brewer–Dobson circulation is very strong in comparison to the HS simulation with both increased upwelling and downwelling magnitudes at all locations. This means that the tropical, downward-propagating QBO-like oscillation in SLD needs to overcome the increased resistance of the upwelling mean flow in HSW, which slows the downward descent (under the assumption

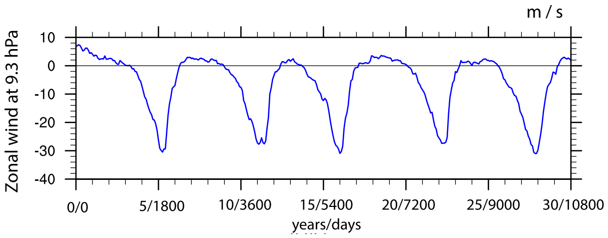

FIG. 15. The 10 800-day time series of the monthly mean zonal-mean zonal wind at the equator (averaged between ±2°) from the SLD HSW simulation at 9.3 hPa. Both the model years and simulation days are provided.

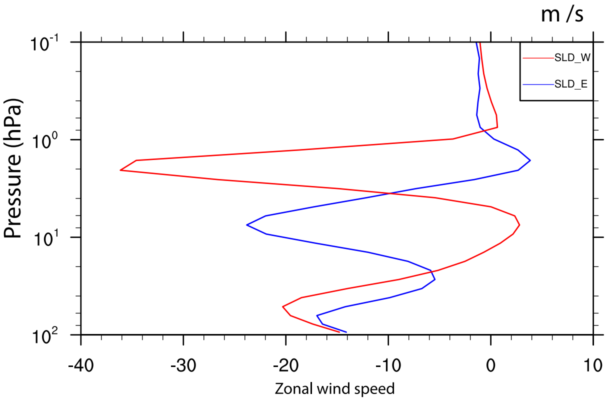

FIG. 16. Vertical 30-month-mean zonal wind profiles at the equator, averaged between ±2°, based on the westerly and easterly SLD composites. The westerly QBO phase composite (SLD_W) is shown in red; the easterly QBO phase composite (SLD_E) is shown in blue.

of an identical wave forcing) and thereby lengthens the QBO period. However, it is also feasible that the presence of the polar jets in HSW impacts the wave activity in all regions and therefore modifies the wave–mean flow interactions in the tropics. This will need to be investigated further in a separate paper. Here, the focus of our investigations lies on the wave activity and the wave–mean flow interactions during the different QBO phases and their interactions with SSWs. This evaluates whether systematic differences between the westerly and easterly QBO branches are present and whether the Holton–Tan relationship holds, which connects the high-latitude wave activity and the QBO phases. The next subsection defines these easterly and easterly QBO episodes in SLD.

c. *Definition of the QBO phases in SLD*

A clearer picture of SLD's QBO-like oscillation is provided in Fig. 15, which shows the 10 800-day time series of the monthly mean zonal-mean zonal wind at the equator at 9.3 hPa. We use this relatively high-lying level to define the onset time of a QBO phase instead of the often used lower-lying positions between 20 and 40 hPa (Baldwin et al. 2001) since the idealized QBO in the HSW simulation is located higher up than the QBO in nature. Whenever the zonal wind is positive in Fig. 15 the westerly phase is recorded. A negative zonal wind at 9.3 hPa characterizes the easterly phase. For the following analysis, 6-month sequences of each QBO cycle (five cycles in total) are recorded during the westerly and easterly phases. The data around the QBO phase-transitioning stage at 9.3 hPa are avoided. The vertical profiles of these 30-month-mean zonal-mean zonal winds at the equator are shown in Fig. 16, which display the westerly and easterly composite phases in red and blue, respectively. On average, the easterly wind amplitude is much stronger than the westerly wind amplitude as it is also typical for the observed QBO. These composites form the basis for the subsequent TEM analysis.

d. *QBO and SSW interactions: Wave fluxes*

A TEM analysis of the SLD model sheds light on the potential interactions between the QBO phases and the strength of the wave fluxes in the midlatitudes and polar regions. The question is whether the easterly QBO phase supports more poleward-oriented waves and thereby potentially more SSWs. The corresponding E–P vector analysis for both the westerly and easterly QBO composites is shown in Fig. 17 with the overlaid zonal-mean zonal wind composites in color. The E–P flux vectors are scaled as in section 3d. Figures 17a,b show the E–P flux vectors during the westerly and easterly phases, respectively. Upward and equatorward E–P flux vectors are observed in the subtropical and midlatitudinal troposphere below 200 hPa and similarly in the midlatitudinal stratosphere during both QBO phases, which indicates the equatorward propagation of waves. The differences between the two figures are subtle and are examined in Fig. 17c.

Figure 17c depicts the E–P vector difference using the westerly phase E–P flux field minus the easterly phase E–P flux field; the colored contours are also the westerly phase zonal-mean zonal wind minus the easterly phase zonal-mean zonal wind. The vector differences in the subtropics and midlatitudes in the lower troposphere (below 200 hPa) show that the average upward wave activity during the easterly phase is stronger than the upward wave activity during the westerly phase, which lets the vector difference point downward. In the tropical stratosphere, stacked easterly and westerly zonal wind differences are observed that are consistent with the analysis from observational data by Naoe and Shibata (2010). Equatorward E–P flux vector differences are present in the stratospheric

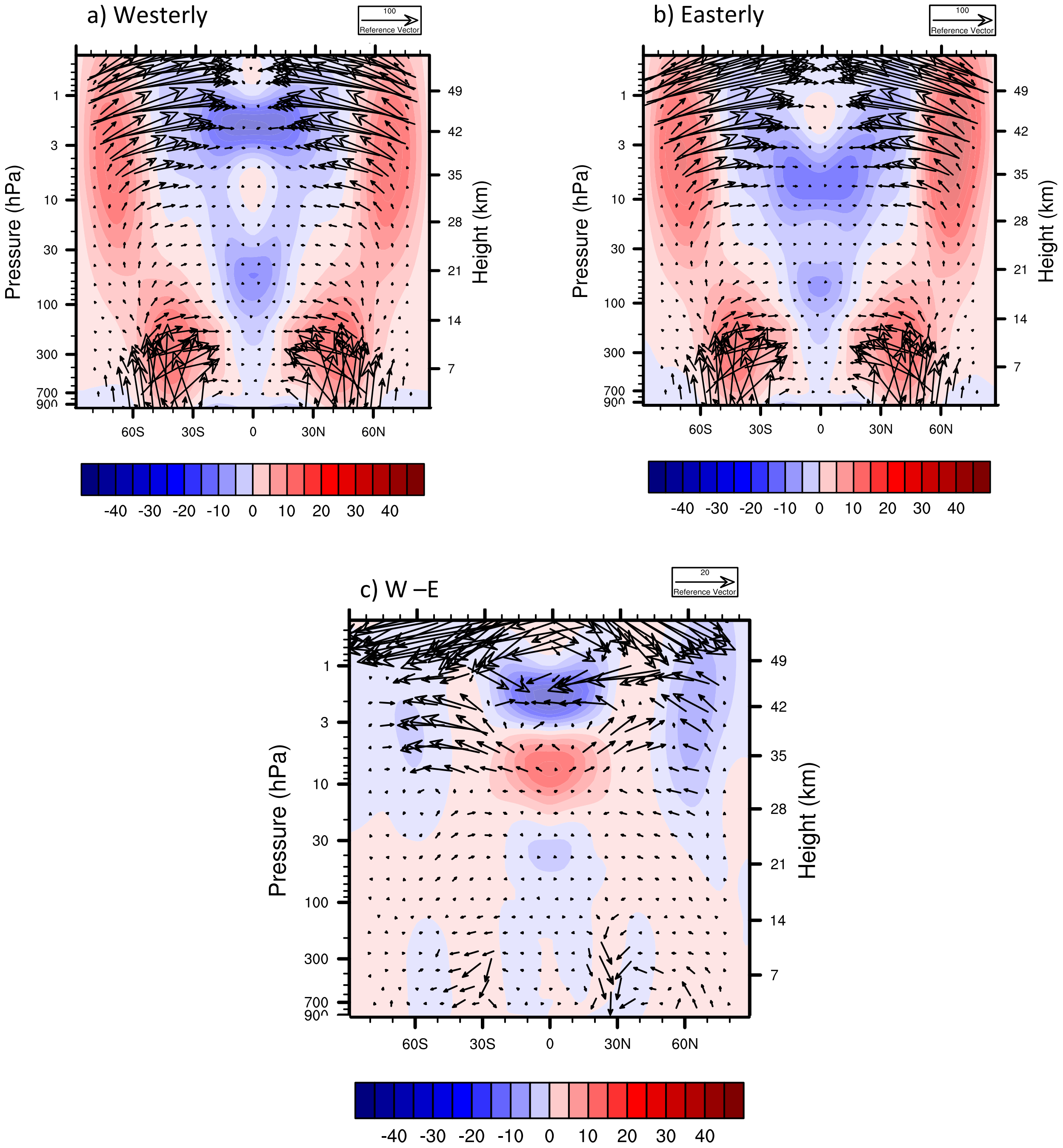

FIG. 17. The 30-month-mean zonal-mean scaled E–P flux vectors ($m^2 s^{-2}$) for westerly and easterly QBO phase composites of the SLD model, overlaid by the corresponding zonal-mean zonal wind in color ($m s^{-1}$): (a) westerly phase, (b) easterly phase, and (c) difference (westerly − easterly). Vectors are scaled following the method in section 3d.

region equatorward of 60° latitude between 10 and 50 hPa in Fig. 17c, which means that the equatorward wave fluxes during the westerly QBO phase are bigger than the equatorward fluxes during the easterly QBO phase. This suggests that the wave–mean flow interactions are more confined to the extratropical and polar regions during the easterly QBO phase and thereby provides some support for the Holton–Tan mechanism. The latter was derived on the basis of lower- to mid-stratospheric observational data at 50 hPa. The analysis at this position cannot be exactly replicated here since the model QBO lies higher than the observed

QBO. Overall, the vector differences are small in this mid-stratospheric region, which invites further investigations of the Holton–Tan effect in the future. In the upper stratosphere between 2 and 10 hPa, the flow characteristics change. Now the vector differences in Fig. 17c point poleward in the tropics and midlatitudes. This indicates that the waves are more confined to the extratropical regions in the westerly QBO phase than in the easterly phase. This is caused by the dominant presence of the tropical easterlies above 5 hPa in Fig. 17a, which diminishes the intrusion of waves into the tropical regions during the westerly QBO phase.

6. Conclusions

This paper analyzed sudden stratospheric warmings and their interactions with the tropical QBO in an ensemble of four idealized dry GCM dynamical cores, which were driven by the Held–Suarez–Williamson forcing. The forcing provides a Newtonian temperature relaxation mimicking radiation and low-level Rayleigh friction mimicking the boundary layer mixing. This forcing thereby replaces the complex physics package of the CAM5 GCM and does not contain processes like moisture, seasonal cycles, or topography. All four CAM5 dynamical cores SLD, EUL, FV, and SE are forced in identical ways with identical vertical grid spacings and very similar horizontal resolutions around 2°. Nevertheless, the results demonstrate that the stratospheric circulations are very different. In particular, the paper focuses on SSWs and their interactions with QBO-like oscillations in long 10 800-day HSW simulations and analyzes the causes and effects of the differences.

First, a single major SSW event in the SLD dynamical core has been highlighted to assess the realism of the idealized HSW simulations. It was shown that the zonal-mean westerly jet with an amplitude of about 30 $\mathrm{m\,s^{-1}}$ at 60°N and 10 hPa is capable of reversing to an easterly flow over short time periods of order 5–15 days, which is a characteristic feature of major warmings. Likewise, the polar stratospheric temperature increases from 205 to 240 K during the same time period. A comprehensive wave analysis has been provided to show that upward-propagating planetary waves, especially with wavenumbers 1 and 2, are the important SSW driving mechanisms, with a dominant wavenumber 1 prior to the SSW event and a more dominant wavenumber-2 forcing during and after the split-vortex event. This establishes that SSWs and their associated wave–mean flow interactions in the HSW simulations have quite realistic attributes even in the absence of typical wave triggering mechanisms like moisture processes, land–sea masks, or topography.

Second, the dynamical core intercomparison reveals that only SLD is capable of producing major warmings during the 10 800-day simulation period. The other three dynamical cores only trigger minor warmings. Two effects contribute to this difference. On the one hand, the assessment of SLD's climatology shows that its polar stratospheric temperatures are warmer. This leads to weaker latitudinal temperature gradients and weaker polar jets in SLD. As a consequence, weaker wave forcings are required to heat SLD's polar cap and collapse–reverse the polar jet. On the other hand, SLD's wave–mean flow interactions are more vigorous in the stratosphere. The corresponding TEM climatology shows that SLD's westward wave forcing of the zonal-mean zonal flow in the midlatitudinal stratosphere is a factor of about 2–3 bigger than the forcing in the other models, which supports more frequent SSWs in SLD. While the SLD dynamical core is not the default numerical scheme at NCAR, designs like the SLD dynamical core are used today for weather prediction applications. For example, the Integrated Forecast System (IFS; weather forecast model used by ECMWF) and the Global Forecast System [GFS; used by the U.S. National Weather Service and the National Centers for Environmental Predictions (NCEP)] have a very similar SLD-like dynamical core. Therefore, our findings for NCAR's SLD dynamical core may provide relevant pointers for similar investigations with these models.

Third, it was demonstrated that both spontaneous QBO-like oscillations and SSWs can coexist in the idealized SLD simulations, which provides a unique tool for studying the interactions between QBO and SSW processes. TEM analyses were performed for composites of easterly and westerly QBO phases. They provide some support of the Holton–Tan mechanism, which suggests that upward-propagating waves are more confined to the extratropics and polar regions during the easterly QBO phases. This has the potential to favor more SSWs during the easterly QBO time periods. However, the E–P flux vector differences in the lower to midstratosphere were small, which lays the basis for future investigations of the Holton–Tan relationship in idealized simulations.

Acknowledgments. The authors thank the reviewers for their helpful suggestions. This work was supported by the U.S. Department of Energy (DoE), Office of Science, Award DE-SC0006684. We acknowledge the high-performance computing support from Yellowstone (ark:/85065/d7wd3xhc) provided by NCAR's Computational and Information Systems Laboratory, sponsored by the National Science Foundation.

REFERENCES

Andrews, D. G., J. D. Mahlman, and R. W. Sinclair, 1983: Eliassen-Palm diagnostics of wave–mean flow interaction in the GFDL ''SKYHI'' general circulation model. *J. Atmos. Sci.*, **40**, 2768–2784, doi:10.1175/1520-0469(1983)040<2768:ETWATM>2.0.CO;2.

——, J. R. Holton, and C. B. Leovoy, 1987: *Middle Atmosphere Dynamics*. International Geophysics Series, Vol. 40, Academic Press, 489 pp.

Anstey, J. A., and T. G. Shepherd, 2014: High-latitude influence of the quasi-biennial oscillation. *Quart. J. Roy. Meteor. Soc.*, **140**, 1–21, doi:10.1002/qj.2132.

——, ——, and J. F. Scinocca, 2010: Influence of the quasi-biennial oscillation on the extratropical winter stratosphere in an atmospheric general circulation model and in reanalysis data. *J. Atmos. Sci.*, **67**, 1402–1419, doi:10.1175/2009JAS3292.1.

Asselin, R., 1972: Frequency filter for time integrations. *Mon. Wea. Rev.*, **100**, 487–490, doi:10.1175/1520-0493(1972)100<0487:FFFTI>2.3.CO;2.

Baldwin, M. P., and T. J. Dunkerton, 1999: Propagation of the Arctic Oscillation from the stratosphere to the troposphere. *J. Geophys. Res.*, **104**, 30 937–30 946, doi:10.1029/1999JD900445.

——, and ——, 2001: Stratospheric harbingers of anomalous weather regimes. *Science*, **294**, 581–584, doi:10.1126/science.1063315.

——, and Coauthors, 2001: The quasi-biennial oscillation. *Rev. Geophys.*, **39**, 179–229, doi:10.1029/1999RG000073.

Bancalá, S., K. Krüger, and M. Giorgetta, 2012: The preconditioning of major sudden stratospheric warmings. *J. Geophys. Res.*, **117**, D04101, doi:10.1029/2011JD016769.

Butler, A. H., D. J. Seidel, S. C. Hardiman, N. Butchart, T. Birner, and A. Match, 2015: Defining sudden stratospheric warmings. *Bull. Amer. Meteor. Soc.*, **96**, 1913–1928, doi:10.1175/BAMS-D-13-00173.1.

Charlton, A. J., and L. M. Polvani, 2007: A new look at stratospheric sudden warmings. Part I: Climatology and modeling benchmarks. *J. Climate*, **20**, 449–469, doi:10.1175/JCLI3996.1.

——, and Coauthors, 2007: A new look at stratospheric sudden warmings. Part II: Evaluation of numerical model simulations. *J. Climate*, **20**, 470–488, doi:10.1175/JCLI3994.1.

Coy, L., and S. Pawson, 2015: The major stratospheric sudden warming of January 2013: Analyses and forecasts in the GEOS-5 data assimilation system. *Mon. Wea. Rev.*, **143**, 491–510, doi:10.1175/MWR-D-14-00023.1.

Dennis, J., and Coauthors, 2012: CAM-SE: A scalable spectral element dynamical core for the Community Atmosphere Model. *Int. J. High Perform. Comput. Appl.*, **26**, 74–89, doi:10.1177/1094342011428142.

Domeisen, D. I., L. Sun, and G. Chen, 2013: The role of synoptic eddies in the tropospheric response to stratospheric variability. *Geophys. Res. Lett.*, **40**, 4933–4937, doi:10.1002/grl.50943.

Edmon, H. J., Jr., B. J. Hoskins, and M. E. McIntyre, 1980: Eliassen-Palm cross sections for the troposphere. *J. Atmos. Sci.*, **37**, 2600–2616, doi:10.1175/1520-0469(1980)037<2600:EPCSFT>2.0.CO;2.

Erlebach, P., U. Langematz, and S. Pawson, 1996: Simulations of stratospheric sudden warmings in the Berlin troposphere-stratosphere-mesosphere GCM. *Ann. Geophys.*, **14**, 443–463, doi:10.1007/s00585-996-0443-6.

Garfinkel, C. I., T. A. Shaw, D. L. Hartmann, and D. W. Waugh, 2012: Does the Holton–Tan mechanism explain how the quasi-biennial oscillation modulates the Arctic polar vortex? *J. Atmos. Sci.*, **69**, 1713–1733, doi:10.1175/JAS-D-11-0209.1.

Gerber, E. P., and L. M. Polvani, 2009: Stratosphere–troposphere coupling in a relatively simple AGCM: The importance of stratospheric variability. *J. Climate*, **22**, 1920–1933, doi:10.1175/2008JCLI2548.1.

Grose, W. L., and K. V. Haggard, 1981: Numerical simulation of a sudden stratospheric warming with a three-dimensional, spectral, quasi-geostrophic model. *J. Atmos. Sci.*, **38**, 1480–1497, doi:10.1175/1520-0469(1981)038<1480:NSOASS>2.0.CO;2.

Held, I. M., and M. J. Suarez, 1994: A proposal for the intercomparison of the dynamical cores of atmospheric general circulation models. *Bull. Amer. Meteor. Soc.*, **75**, 1825–1830, doi:10.1175/1520-0477(1994)075<1825:APFTIO>2.0.CO;2.

Hitchcock, P., and I. R. Simpson, 2014: The downward influence of stratospheric sudden warmings. *J. Atmos. Sci.*, **71**, 3856–3876, doi:10.1175/JAS-D-14-0012.1.

Holton, J. R., 1976: A semi-spectral numerical model for wave-mean flow interactions in the stratosphere: Application to sudden stratospheric warmings. *J. Atmos. Sci.*, **33**, 1639–1649, doi:10.1175/1520-0469(1976)033<1639:ASSNMF>2.0.CO;2.

——, and H.-C. Tan, 1980: The influence of the equatorial quasi-biennial oscillation on the global circulation at 50 mb. *J. Atmos. Sci.*, **37**, 2200–2208, doi:10.1175/1520-0469(1980)037<2200:TIOTEQ>2.0.CO;2.

Jablonowski, C., and D. L. Williamson, 2011: The pros and cons of diffusion, filters, and fixers in atmospheric general circulation models. *Numerical Techniques for Global Atmospheric Models*, P. H. Lauritzen et al., Eds., Lecture Notes in Science and Engineering, Vol. 80, Springer, 381–493.

Jucker, M., S. Fueglistaler, and G. K. Vallis, 2013: Maintenance of the stratospheric structure in an idealized general circulation model. *J. Atmos. Sci.*, **70**, 3341–3358, doi:10.1175/JAS-D-12-0305.1.

——, ——, and ——, 2014: Stratospheric sudden warmings in an idealized GCM. *J. Geophys. Res. Atmos.*, **119**, 11 054–11 064, doi:10.1002/2014JD022170.

Jung, T., and J. Barkmeijer, 2006: Sensitivity of the tropospheric circulation to changes in the strength of the stratospheric polar vortex. *Mon. Wea. Rev.*, **134**, 2191–2207, doi:10.1175/MWR3178.1.

——, and M. Leutbecher, 2007: Performance of the ECMWF forecasting system in the Arctic during winter. *Quart. J. Roy. Meteor. Soc.*, **133**, 1327–1340, doi:10.1002/qj.99.

Kodera, K., H. Mukougawa, and A. Fujii, 2013: Influence of the vertical and zonal propagation of stratospheric planetary waves on tropospheric blockings. *J. Geophys. Res. Atmos.*, **118**, 8333–8345, doi:10.1002/jgrd.50650.

Krüger, K., B. Naujokat, and K. Labitzke, 2005: The unusual midwinter warming in the Southern Hemisphere stratosphere 2002: A comparison to Northern Hemisphere phenomena. *J. Atmos. Sci.*, **62**, 603–613, doi:10.1175/JAS-3316.1.

Kushner, P. J., and L. M. Polvani, 2005: A very large, spontaneous stratospheric sudden warming in a simple AGCM: A prototype for the Southern Hemisphere warming of 2002? *J. Atmos. Sci.*, **62**, 890–897, doi:10.1175/JAS-3314.1.

Labitzke, K., 1981: The amplification of height wave 1 in January 1979: A characteristic precondition for the major warming in February. *Mon. Wea. Rev.*, **109**, 983–989, doi:10.1175/1520-0493(1981)109<0983:TAOHWI>2.0.CO;2.

Limpasuvan, V., D. W. J. Thompson, and D. L. Hartmann, 2004: The life cycle of the Northern Hemisphere sudden stratospheric warmings. *J. Climate*, **17**, 2584–2597, doi:10.1175/1520-0442(2004)017<2584:TLCOTN>2.0.CO;2.

Lin, S.-J., 2004: A ''vertically Lagrangian'' finite-volume dynamical core for global models. *Mon. Wea. Rev.*, **132**, 2293–2307, doi:10.1175/1520-0493(2004)132<2293:AVLFDC>2.0.CO;2.

——, and R. B. Rood, 1996: Multidimensional flux-form semi-Lagrangian transport scheme. *Mon. Wea. Rev.*, **124**, 2046–2070, doi:10.1175/1520-0493(1996)124<2046:MFFSLT>2.0.CO;2.

Lu, H., T. J. Bracegirdle, T. Phillips, A. Bushell, and L. Gray, 2014: Mechanisms for the Holton-Tan relationship and its decadal variation. *J. Geophys. Res. Atmos.*, **119**, 2811–2830, doi:10.1002/2013JD021352.

Manney, G. L., and Coauthors, 2005: Simulations of dynamics and transport during the September 2002 Antarctic major warming. *J. Atmos. Sci.*, **62**, 690–707, doi:10.1175/JAS-3313.1.

Manzini, E., and L. Bengtsson, 1996: Stratospheric climate and variability from a general circulation model and observations. *Climate Dyn.*, **12**, 615–639, doi:10.1007/BF00216270.

Marshall, A. G., and A. A. Scaife, 2010: Improved predictability of stratospheric sudden warming events in an atmospheric general circulation model with enhanced stratospheric resolution. *J. Geophys. Res.*, **115**, D16114, doi:10.1029/2009JD012643.

Martineau, P., and S.-W. Son, 2013: Planetary-scale wave activity as a source of varying tropospheric response to stratospheric sudden warming events: A case study. *J. Geophys. Res. Atmos.*, **118**, 10 994–11 006, doi:10.1002/jgrd.50871.

Martius, O., L. M. Polvani, and H. C. Davies, 2009: Blocking precursors to stratospheric sudden warming events. *Geophys. Res. Lett.*, **36**, L14806, doi:10.1029/2009GL038776.

Matsuno, T., 1971: A dynamical model of the stratospheric sudden warming. *J. Atmos. Sci.*, **28**, 1479–1494, doi:10.1175/1520-0469(1971)028<1479:ADMOTS>2.0.CO;2.

McCalpin, J. D., 1988: A quantitative analysis of the dissipation inherent in semi-Lagrangian advection. *Mon. Wea. Rev.*, **116**, 2330–2336, doi:10.1175/1520-0493(1988)116<2330:AQAOTD>2.0.CO;2.

McLandress, C., and T. G. Shepherd, 2009: Impact of climate change on stratospheric sudden warmings as simulated by the Canadian Middle Atmosphere Model. *J. Climate*, **22**, 5449–5463, doi:10.1175/2009JCLI3069.1.

Naito, Y., and S. Yoden, 2006: Behavior of planetary waves before and after stratospheric sudden warming events in several phases of the equatorial QBO. *J. Atmos. Sci.*, **63**, 1637–1649, doi:10.1175/JAS3702.1.

——, M. Taguchi, and S. Yoden, 2003: A parameter sweep experiment on the effects of the equatorial QBO on stratospheric sudden warming events. *J. Atmos. Sci.*, **60**, 1380–1394, doi:10.1175/1520-0469(2003)060<1380:APSEOT>2.0.CO;2.

Naoe, H., and K. Shibata, 2010: Equatorial quasi-biennial oscillation influence on northern winter extratropical circulation. *J. Geophys. Res.*, **115**, D19102, doi:10.1029/2009JD012952.

Naujokat, B., K. Krüger, K. Matthes, J. Hoffmann, M. Kunze, and K. Labitzke, 2002: The early major warming in December 2001—Exceptional? *Geophys. Res. Lett.*, **29**, 2023, doi:10.1029/2002GL015316.

Neale, R. B., and Coauthors, 2010: Description of the NCAR Community Atmosphere Model (CAM 5.0). National Center for Atmospheric Research Tech. Note NCAR/TN-486+STR, 282 pp. [Available online at http://www.cesm.ucar.edu/models/cesm1.0/cam/docs/description/cam5_desc.pdf.]

O'Neill, A., 1980: The dynamics of stratospheric warmings generated by a general circulation model of the troposphere and stratosphere. *Quart. J. Roy. Meteor. Soc.*, **106**, 659–690, doi:10.1002/qj.49710645002.

——, 2003: Stratospheric sudden warmings. *Encyclopedia of Atmospheric Sciences*, J. R. Holton, J. A. Pyle, and J. A. Curry, Eds., Elsevier, 1342–1353.

Richter, J. H., K. Matthes, N. Calvo, and L. J. Gray, 2011: Influence of the quasi-biennial oscillation and El Niño–Southern Oscillation on the frequency of sudden stratospheric warmings. *J. Geophys. Res.*, **116**, D20111, doi:10.1029/2011JD015757.

Scaife, A. A., D. R. Jackson, R. Swinbank, N. Butchart, H. E. Thornton, M. Keil, and L. Henderson, 2005: Stratospheric vacillations and the major warming over Antarctica in 2002. *J. Atmos. Sci.*, **62**, 629–639, doi:10.1175/JAS-3334.1.

Scherhag, R., 1952: Die explosionsartige stratosphärenerwärmung des spätwinters 1951/52. *Ber. Dtsch. Wetterdienstes*, **38**, 51–63.

Schoeberl, M. R., 1978: Stratospheric warmings: Observations and theory. *Rev. Geophys.*, **16**, 521–538, doi:10.1029/RG016i004p00521.

Scinocca, J. F., and P. H. Haynes, 1998: Dynamical forcing of stratospheric planetary waves by tropospheric baroclinic eddies. *J. Atmos. Sci.*, **55**, 2361–2392, doi:10.1175/1520-0469(1998)055<2361:DFOSPW>2.0.CO;2.

Sheshadri, A., E. P. Gerber, and R. A. Plumb, 2015: Seasonal variability of the polar stratospheric vortex in an idealized AGCM with varying tropospheric wave forcing. *J. Atmos. Sci.*, **72**, 2248–2266, doi:10.1175/JAS-D-14-0191.1.

Sigmond, M., J. F. Scinocca, V. V. Kharin, and T. G. Shepherd, 2013: Enhanced seasonal forecast skill following stratospheric sudden warmings. *Nat. Geosci.*, **6**, 98–102, doi:10.1038/ngeo1698.

Simmons, A. J., and R. Strüfing, 1983: Numerical forecasts of stratospheric warming events using a model with a hybrid vertical coordinate. *Quart. J. Roy. Meteor. Soc.*, **109**, 81–111, doi:10.1002/qj.49710945905.

Sun, L., W. A. Robinson, and G. Chen, 2012: The predictability of stratospheric warming events: More from the troposphere or the stratosphere? *J. Atmos. Sci.*, **69**, 768–783, doi:10.1175/JAS-D-11-0144.1.

Taguchi, M., and S. Yoden, 2002a: Internal interannual variability of the troposphere–stratosphere coupled system in a simple global circulation model. Part I: Parameter sweep experiment. *J. Atmos. Sci.*, **59**, 3021–3036, doi:10.1175/1520-0469(2002)059<3021:IIVOTT>2.0.CO;2.

——, and ——, 2002b: Internal interannual variability of the troposphere–stratosphere coupled system in a simple global circulation model. Part II: Millennium integrations. *J. Atmos. Sci.*, **59**, 3037–3050, doi:10.1175/1520-0469(2002)059<3037:IIVOTT>2.0.CO;2.

——, T. Yamaga, and S. Yoden, 2001: Internal variability of the troposphere–stratosphere coupled system simulated in a simple global circulation model. *J. Atmos. Sci.*, **58**, 3184–3203, doi:10.1175/1520-0469(2001)058<3184:IVOTTS>2.0.CO;2.

Taylor, M. A., and A. Fournier, 2010: A compatible and conservative spectral element method on unstructured grids. *J. Comput. Phys.*, **229**, 5879–5895, doi:10.1016/j.jcp.2010.04.008.

Thompson, D. W. J., and J. M. Wallace, 2001: Regional climate impacts of the Northern Hemisphere annular mode. *Science*, **293**, 85–89, doi:10.1126/science.1058958.

Vial, J., T. J. Osborn, and F. Lott, 2013: Sudden stratospheric warmings and tropospheric blockings in a multi-century simulation of the IPSL-CM5A coupled climate model. *Climate Dyn.*, **40**, 2401–2414, doi:10.1007/s00382-013-1675-2.

Watson, P. A., and L. J. Gray, 2014: How does the quasi-biennial oscillation affect the stratospheric polar vortex? *J. Atmos. Sci.*, **71**, 391–409, doi:10.1175/JAS-D-13-096.1.

Wei, K., W. Chen, and R. Huang, 2007: Association of tropical Pacific sea surface temperatures with the stratospheric Holton-Tan Oscillation in the Northern Hemisphere winter. *Geophys. Res. Lett.*, **34**, L16814, doi:10.1029/2007GL030478.

Whitehead, J. P., C. Jablonowski, R. B. Rood, and P. H. Lauritzen, 2011: A stability analysis of divergence damping on a latitude–longitude grid. *Mon. Wea. Rev.*, **139**, 2976–2993, doi:10.1175/2011MWR3607.1.

——, ——, J. Kent, and R. B. Rood, 2015: Potential vorticity: Measuring consistency between GCM dynamical cores and tracer advection schemes. *Quart. J. Roy. Meteor. Soc.*, **141**, 739–751, doi:10.1002/qj.2389.

Williamson, D. L., J. G. Olson, and B. A. Boville, 1998: A comparison of semi-Lagrangian and Eulerian tropical climate simulations. *Mon. Wea. Rev.*, **126**, 1001–1012, doi:10.1175/1520-0493(1998)126<1001:ACOSLA>2.0.CO;2.

WMO CAS, 1978: WMO Commission for Atmospheric Sciences. Abridged Final Rep. of the Seventh Session, WMO 509, 113 pp.

Woollings, T., A. Charlton-Perez, S. Ineson, A. G. Marshall, and G. Masato, 2010: Associations between stratospheric variability and tropospheric blocking. *J. Geophys. Res.*, **115**, D06108, doi:10.1029/2009JD012742.

Yao, W., and C. Jablonowski, 2013: Spontaneous QBO-like oscillations in an atmospheric model dynamical core. *Geophys. Res. Lett.*, **40**, 3772–3776, doi:10.1002/grl.50723.

——, and ——, 2015: Idealized quasi-biennial oscillations in an ensemble of dry GCM dynamical cores. *J. Atmos. Sci.*, **72**, 2201–2226, doi:10.1175/JAS-D-14-0236.1.